

Automated Frequency Locking via Spectroscopy on trapped $^{40}\text{Ca}^+$ Ions

Master Thesis

zur Erlangung des Mastergrades an der

Fakultät für Mathematik, Informatik und Physik
der Leopold-Franzens-Universität Innsbruck
vorgelegt von

Marc Georg Bußjäger, BSc

durchgeführt am Institut für Experimentalphysik

unter der Leitung von
Univ.-Prof. Dr. Rainer Blatt

Innsbruck am 9. August 2020

Abstract

Over the last decade, quantum experiments have grown considerably in complexity. In order to not divert focus from research itself, as many subroutines of the experiments as possible have to be automated. In the given quantum experiment, optical qubits are encoded in trapped $^{40}\text{Ca}^+$ ions. Within the scope of this thesis, the frequency of the laser system driving the qubit transitions is stabilized to the transitions of the trapped ions. This is achieved by periodically performing spectroscopy on the trapped ions, followed by frequentist as well as Bayesian data analysis approaches. In order to automate these tasks, a corresponding computer program is integrated into the experiment control system. Furthermore, a remote control interface is developed, allowing the remote submission of quantum algorithms written in the established quantum description languages Cirq developed by Google LLC, and OpenPulse developed by the International Business Machines Corporation (IBM).

Kurzfassung

Im Laufe des letzten Jahrzehntes nahm die Komplexität von Quantenexperimenten erheblich zu. Das Automatisieren so vieler Subroutinen dieser Experimente wie möglich kann verhindern, dass aufgrund dieses Trends das Hauptaugenmerk von der Forschung selbst weg gelenkt wird. Im vorliegenden Quantenexperiment werden optische Qubits verwendet, welche auf gefangenen $^{40}\text{Ca}^+$ Ionen kodiert sind. Im Rahmen dieser Arbeit, wird die Frequenz des Qubit-Übergänge treibenden Lasersystems auf die Übergänge der gefangenen Ionen stabilisiert. Dies wird durch periodische Spektroskopie an den gefangenen Ionen, gefolgt von frequentistischen sowie Bayes'schen Datenanalyseansätzen, erreicht. Durch die Integration eines entsprechenden Computerprogramms in das Kontrollsystem des Experimentes, werden diese Arbeitsschritte automatisiert. Des Weiteren, wird ein Fernzugriff implementiert, welcher das Einsenden von Quantenalgorithmen ermöglicht. Für die Spezifikation der Quantenalgorithmen werden die bereits etablierten Quantenbeschreibungssprachen Cirq und OpenPulse verwendet, welche respektive von Google LLC und der International Business Machines Corporation (IBM) entwickelt werden.

Contents

1	Introduction	1
2	Theoretical Framework	3
2.1	Trapped $^{40}\text{Ca}^+$ Ions	3
2.2	Ion Trap Quantum Computing	5
2.3	Light-Atom Interaction	8
2.4	Rabi Spectroscopy	10
2.5	Ramsey Spectroscopy	12
3	Frequency Stabilization	15
3.1	Stable References	15
3.2	Rabi Spectroscopy	17
3.3	Ramsey Spectroscopy	20
4	Bayesian Inference	23
4.1	Frequentism	23
4.2	Bayesianism	24
4.3	Bayesianism vs. Least Squares Minimization	35
5	Experimental Results	39
5.1	Rabi Spectroscopy	39
5.2	Adaptive Bayesian Ramsey Spectroscopy	41
5.3	Variation of Drifts	46
6	Simplified Quantum Computer Control	51
6.1	Quantum Control Program	51
6.2	Quantum Programming Languages	54
6.3	Remote Access	63
7	Summary and Outlook	65
	Bibliography	68

Chapter 1

Introduction

Since their invention, reaching back to 1941 when the first functional digital computer Zuse Z3 has been created [1], computers have been a revolutionizing tool. Science and technology have expanded, as computers allow numerical simulations of complex phenomena, like e.g. the collision of galaxies [2]. The everyday life is revolutionized by computers, considering inventions like self-driving cars [3]. Furthermore, computers simplify the storage of and access to scientific knowledge, as well as have revolutionized international communication and collaboration since the advent of the internet in the 1960s [4].

The computational power of processors has increased almost exponentially with time since 1980, leading to the formulation of Moore's law [5]. However, it is expected that this development will slow down in the near future, mainly due to design and power limitations of processors [6]. In order to maintain such an exponential growth, and to satisfy the demand for increasingly more powerful processors, new approaches to perform computations are therefore necessary [7]. A revolutionizing idea, is the introduction of quantum computers. Classical computers are restricted to perform their computations in a binary language using bits. A quantum computer is based on quantum bits (qubits), with which the complexity of quantum mechanical states can be exploited as a basis for computations [8]. This leads to algorithms that can perform certain tasks significantly faster on a quantum computer than on classical computer [9, 10].

Quantum computers rely on exotic quantum states, and are thus vulnerable to noisy environments [11]. Furthermore, the preparation, manipulation and read-out of information stored in quantum mechanical states is subject to noise, limiting the practical usability of a quantum computer [8, 12]. As the performance of a classical computer is limited by the amount of its working memory, the complexity of the algorithms that can be executed on a quantum computer is limited by the amount of physical qubits that are available to perform calculations on.

Current quantum computers form a group called Noisy Intermediate-Scale Quantum (NISQ) computers [13]. For most NISQ computers, the precise and simultaneous control of many experimental parameters is required to perform complex calculations and to achieve a desired level of accuracy and reliability [14]. This leads to many subroutines that increase the complexity of the experiment. The automation of said subroutines can help to achieve a more accurate control over the experimental param-

eters, which in turn increases the overall performance of the experiment.

The NISQ computer on which the work of this thesis is performed on is a trapped ion quantum computer [15] that will be elaborated on in chapter 2. Qubits are encoded in the $4^2S_{1/2}$ to $3^2D_{5/2}$ transitions of trapped calcium ions. Quantum gate operations can be performed using a laser system operating at a wavelength of 729 nm [15]. The frequency of this laser system has to be precisely tuned and stabilized to the qubit transition frequency in order to facilitate quantum gate operations. Within the scope of this thesis, methods are presented to automatically stabilize the frequency of said laser system using the atomic transition frequency of the qubit transition itself as a reference. These methods utilize spectroscopy experiments and data analysis with different mathematical approaches, the details of which will be explained and compared in the chapters 3 and 4. The automated, continuous re-calibration of the laser system is the basis for quantum gate operations. Furthermore, less time and effort is lost with respect to performing the corresponding spectroscopy and re-calibration tasks manually, and the reproducibility of the experimental data is increased. Last but not least, the integration of automation routines is a step towards a reliable 24/7 operation of the system, facilitating e.g. long measurements. The achieved stability via said automated re-calibration is investigated in chapter 5.

In chapter 6 quantum algorithm description languages are introduced, simplifying the user interface of the experiment control system as well as the communication between its components. The introduction of such languages leads to the implementation of an interface, that allows the submission of quantum algorithms from remote locations, facilitating the communication and cooperation with collaborators across the world. The languages chosen for this interface are the already established quantum description languages Cirq and OpenPulse, which are developed by Google LLC and the International Business Machines Corporation (IBM) respectively. The interface itself is not specific to a single programming language.

Chapter 2

Theoretical Framework

In this chapter an introduction over the theoretical foundation of the ion trap experiment is given, starting with the notations and experimental setup in section 2.1. Section 2.2 discusses the major differences between classical and quantum computers and introduces how quantum bits (qubits) can be implemented within the experimental setup. With regard to performing quantum gate operations, the interaction between light and trapped ions is discussed in more detail in section 2.3, motivating how resonant light pulses can be used to implement unitary quantum gate operations. Discussing the effect of a non-resonant light field interacting with atoms, section 2.4 elaborates on the theoretical framework to perform Rabi spectroscopy. Section 2.5 concludes this chapter with introducing the Ramsey sequence providing the theoretical foundation of Ramsey spectroscopy.

2.1 Trapped $^{40}\text{Ca}^+$ Ions

Atoms consist of negatively charged electrons as well as positively charged protons, where the latter, together with neutrally charged neutrons, form the core or nucleus of an atom. An atomic ion is an atom that carries charge. Negatively charged ions i.e. atoms with more electrons than protons are called anions, whereas positively charged ions are called cations. The number of protons in an atom dictates its species. Variations on the number of neutrons are called isotopes. The standard notation for atoms is ${}^A_Z X$, where X is the abbreviation of the element, Z the atomic number which is equal to the number of protons, and A the mass number being the sum of Z and the number of neutrons. As every element has its distinct atomic number, one often drops the subscript Z in this notation. By adding a superscript after X , the charge of the atom is expressed. For singly charged calcium cations of its most abundant natural isotope this gives the notation ${}^{40}_{20}\text{Ca}^+$, or equivalently $^{40}\text{Ca}^+$ when dropping the subscript Z .

With applying light pulses an atom can be excited, changing which orbitals are occupied by its electrons. The atom then has the probability to decay back to the electronic ground state, being the least energetic state available. A change of electronic states is also called transition. The probability to drive such a transition with a light pulse is maximized, when the energy of the light field matches the energy difference between the states. When decaying from an excited state to an energeti-

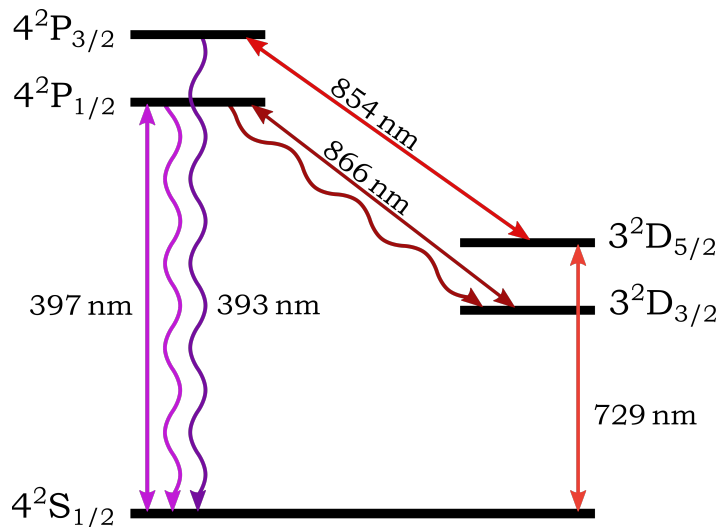


Figure 2.1.1: Level scheme of $^{40}\text{Ca}^+$ including all required laser systems. The electronic states are shown as thick black lines with their energy increasing from bottom to top. The transitions driven by the required laser systems as well as their respective wavelength are represented by arrows. Decay channels are represented by wavy arrows.

cally lower lying state, the atom emits a photon of the corresponding transition frequency. The different electronic states are labeled using the term symbol, given by $n^{2S+1}L_J$, where $n \in \mathbb{N}$ is the principal quantum number, $L \in \{L < n \mid L \in \mathbb{N}_0\}$ is the total orbital momentum quantum number being labeled with S, P, D, F, etc. (continuing alphabetically), $S \in \{S \leq L \mid S \in \mathbb{N}_0\}$ is the total spin quantum number and $J \in \{|L - S| + i \mid i \in \mathbb{N}_0 \wedge (|L - S| + i) < (L + S)\}$ is the total angular momentum quantum number. A level scheme of $^{40}\text{Ca}^+$ including all laser systems required for the quantum computer experiment is shown in figure 2.1.1. Electronic states are depicted as thick lines and are sorted by increasing energy from bottom to top. Quantum gate operations are performed using the $4^2\text{S}_{1/2}$ to $3^2\text{D}_{5/2}$ transition, which can be driven using a laser system operating at a wavelength of 729 nm. The latter state has a comparatively long lifetime in the order of ~ 1 s [16], whereas the $4^2\text{P}_{3/2}$ state has a lifetime of about ~ 7 ns [17]. Thus, the $3^2\text{D}_{5/2}$ to $4^2\text{P}_{3/2}$ transition is used to reset the system to the $4^2\text{S}_{1/2}$ state after an experiment is completed.

In the experimental setup, a linear Paul trap [18], schematically depicted in figure 2.1.2, is used to trap multiple $^{40}\text{Ca}^+$ ions [19]. The trap consists of four blades as well as two end-cap electrodes. Radial confinement is achieved by applying an oscillating voltage to one pair of opposing blades while the other two blades are grounded. Applying a DC voltage to the end-caps leads to axial confinement between the electrodes. The trap is placed inside a vacuum chamber. Neutral calcium atoms are evaporated from an oven and then ionized in the center of the trap via two laser beams at a wavelength of 375 nm and 423 nm respectively, performing a two-step photo-ionization of the atoms [20]. After Doppler cooling [21], the trapped ions form a linear ion crystal in the center of the trapping region. The detection of the trapped ions is based on imaging their fluorescence, by applying a light pulse with a wavelength of 397 nm to the trapping region that is driving the $4^2\text{S}_{1/2}$ to $4^2\text{P}_{1/2}$ transition. The same laser system and transition used for imaging are also used for Doppler cooling. Due to the level struc-

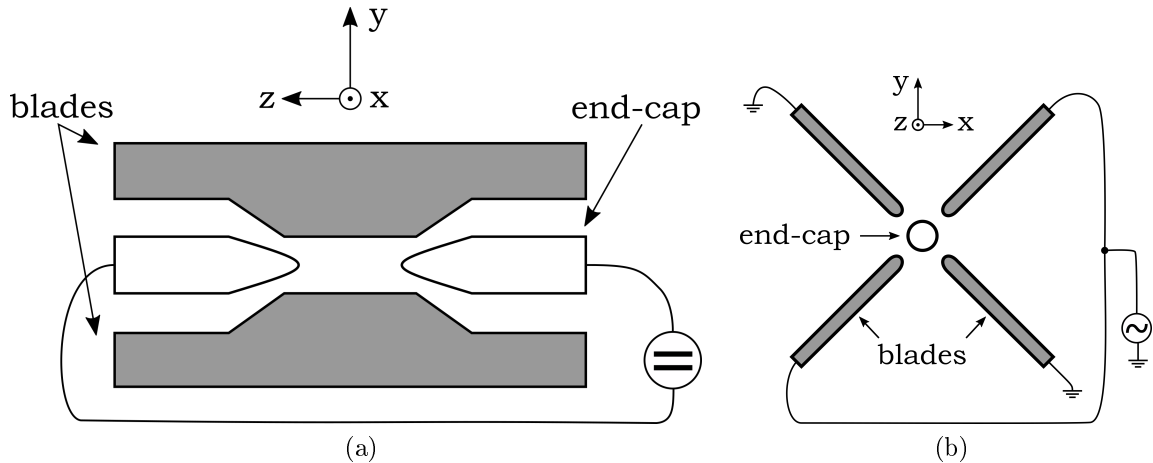


Figure 2.1.2: Front and side view of a linear Paul trap. The trap consists of two opposing end-cap electrodes as well as four blades. (a) The front view shows a DC voltage applied to the two end-cap electrodes, leading to a confinement along the z -axis. (b) Radial confinement, perpendicular to the z -axis is achieved by applying an oscillating voltage to two of the four blades, while setting the others to ground.

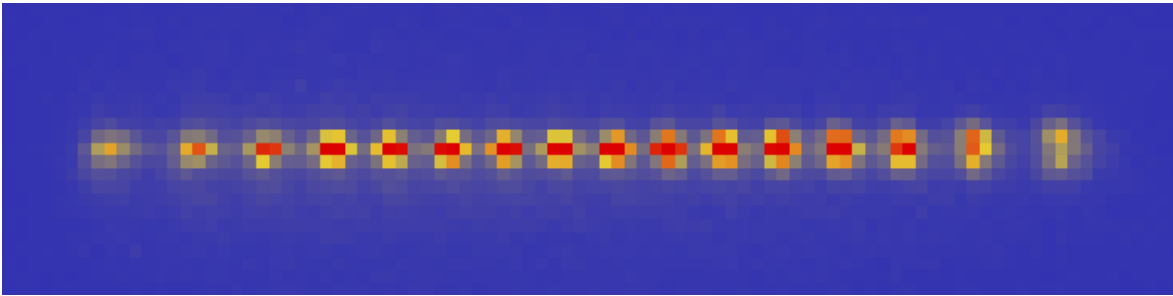


Figure 2.1.3: EMCCD camera picture of 16 trapped ions of the linear Paul trap's central region. As described in section 2.1, trapped $^{40}\text{Ca}^+$ ions emit fluorescence photons that are recorded by an EMCCD camera. The 16 $^{40}\text{Ca}^+$ ions in this picture are Doppler cooled and form a linear ion crystal.

ture of $^{40}\text{Ca}^+$, the $4^2\text{P}_{1/2}$ state can spontaneously decay into the $3^2\text{D}_{3/2}$ state, having a lifetime in the order of ~ 1 s [16]. This would decrease the rate in which fluorescence photons are scattered, making Doppler cooling as well as imaging the photons onto an electron multiplying (EM)CCD camera impossible. Therefore, an additional laser beam is added, to pump out this dark state. At a wavelength of 866 nm, the additional laser beam transfers the populations from the $3^2\text{D}_{3/2}$ state back to the $4^2\text{P}_{1/2}$ state. With the latter state having a lifetime of ~ 7 ns [22], the scattering rate of photons is high enough for an EMCCD camera to detect fluorescence. The resulting imaged fluorescence of 16 trapped ions can be seen in figure 2.1.3.

2.2 Ion Trap Quantum Computing

The main difference between a classical computer and a quantum computer is the fact that a classical one works with bits, whereas a quantum computer works with quantum

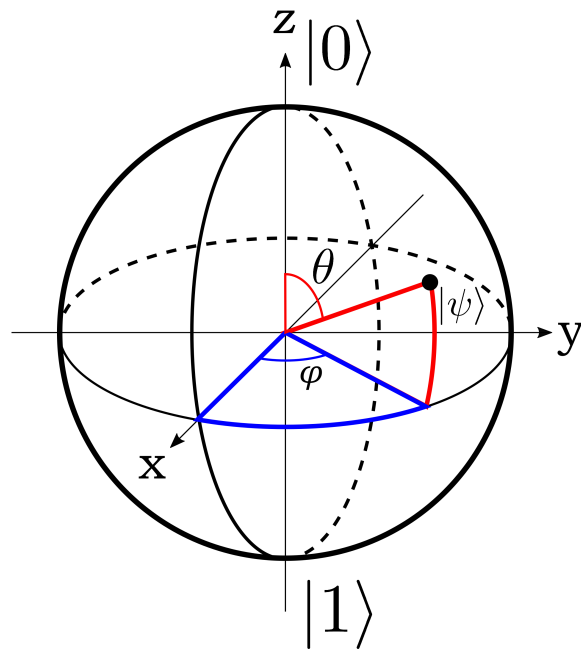


Figure 2.2.1: Bloch sphere. A qubit $|\psi\rangle$ can be represented by a point on the Bloch sphere. The poles of the Bloch sphere represent the orthogonal basis states $|0\rangle$ and $|1\rangle$. Given the angles φ and θ , any qubit can be mapped onto the Bloch sphere.

bits (qubits). A classical bit can either represent the value zero or one, leading to a binary language in which a classical computer performs its calculations. A fitting analogy is a light switch that turns a light bulb on or off. A qubit on the other hand is represented by the quantum mechanical state of a two-level system

$$|\psi\rangle = \alpha |0\rangle + \beta |1\rangle \quad (2.2.1)$$

where the states $|0\rangle$ and $|1\rangle$ are orthogonal basis states spanning a two-dimensional Hilbert space, and $\alpha, \beta \in \mathbb{C}$ with $|\alpha|^2 + |\beta|^2 = 1$. As the overall phase can be set arbitrarily when defining the qubit, equation (2.2.1) can also be written as

$$|\psi\rangle = \cos(\theta/2) |0\rangle + e^{i\varphi} \sin(\theta/2) |1\rangle. \quad (2.2.2)$$

In this form, a qubit can be represented as a point on the Bloch sphere (figure 2.2.1). Continuing the analogy of a bit being a switch that turns a light bulb on and off, a qubit is a switch that is capable of dimming a light bulb, as well as changing its color in a continuous way.

Another important difference between classical bits and qubits is the operations that can be applied to them. The only operations that can be performed on single classical bits, are the identity, which corresponds to leaving them at the state they are prepared in, or performing a bit-flip, where the values zero and one are exchanged with one another. Operations on single qubits however are fundamentally different, as they consist of unitary operations, which correspond to arbitrary rotations of the state on the Bloch sphere. Furthermore, qubits can be entangled with one another, linking their states such that operations on one qubit affect the state of the other. Exploiting

these differences, some problems can be solved in less time on a quantum computer, by applying quantum algorithms such as Grover's [10] or Shor's algorithm [9, 23].

Qubits can be realized in a variety of different physical architectures. In the given ion trap quantum computer, the qubit is defined by selecting two electronic states of a trapped ion. A magnetic field at the position of the trapped ions, leads to a shift in the energy of magnetically sensitive states [24, 25]. This shift from the unperturbed center frequency is called Zeeman effect which is a result of the magnetic moment μ of the electrons interacting with the applied magnetic field. In first order perturbation theory, the frequency shift $\Delta\nu_Z$ resulting from the Zeeman effect can be calculated as [26]

$$\Delta\nu_Z(m_j, g_j) = m_j g_j \frac{\mu_B \cdot B}{\hbar}$$

with m_j being the projection of the corresponding atom's total angular momentum \mathbf{J} along the unit vector \mathbf{e}_j of the applied magnetic field $\mathbf{B} = B \cdot \mathbf{e}_j$, g_j the Landé g-factor of the corresponding state, μ_B the Bohr magneton, and \hbar the reduced Planck constant. For the state $4^2S_{1/2}$ of $^{40}\text{Ca}^+$, the g-factor has been measured as $g_S = 2.00225664$ (9) [27]. The g-factor g_D of the $3^2D_{5/2}$ state can be calculated as $g_D = 1.2$, using [28]

$$g_j = 1 + \frac{j(j+1) + s(s+1) - l(l+1)}{2j(j+1)}$$

where $j = 5/2$ is the total angular momentum quantum number, $s = 1/2$ the spin quantum number, and $l = 2$ the orbital momentum quantum number of the state. The shift $\Delta\nu_Z$ is dependent on the total angular momentum of the corresponding state and therefore leads to the Zeeman splitting of all states with a $j \neq 0$, resulting in $2 \cdot j + 1$ Zeeman sub-levels of the respective state. In the case of the $4^2S_{1/2}$ and $3^2D_{5/2}$ states, all resulting Zeeman sub-levels are depicted in figure 2.2.2. The shown transitions are labeled with the notation $(m_j(\text{S}), m_j(\text{D}))$, with $m_j(\text{S})$ and $m_j(\text{D})$ corresponding to the projection m_j of the $4^2S_{1/2}$ and the $3^2D_{5/2}$ state's total angular momentum respectively. The qubit is then defined as the $(-1/2, -1/2)$ transition between the corresponding Zeeman sub-levels of a trapped $^{40}\text{Ca}^+$ ion's $4^2S_{1/2}$ to $3^2D_{5/2}$ transition. This choice has been made, as the transitions $(-1/2, -1/2)$ and $(+1/2, +1/2)$ have the lowest sensitivity to the magnetic field strength of all transitions shown in figure 2.2.2, and $4^2S_{1/2}(m_j(\text{S}) = -1/2)$ is the ground state of the ion. Using the definition in equation (2.2.1), the state $4^2S_{1/2}(m_j(\text{S}) = -1/2)$ thereby corresponds to the state $|0\rangle$ and $3^2D_{5/2}(m_j(\text{D}) = -1/2)$ to the state $|1\rangle$.

Measuring the values α and β of a qubit is achieved using a technique called electron shelving [29]. If a qubit as described above is in the ground state $4^2S_{1/2}$, the atom can be excited to the higher lying $4^2P_{1/2}$ state via shining resonant light onto the ion, using a laser system that operates at a wavelength of 397 nm. The atom will then decay back to the ground state, closing the cyclic transition and spontaneously emitting a fluorescence photon that can be detected. If the state of the atom is projected into the $3^2D_{5/2}$ state, applying a 397 nm wavelength light pulse does not excite the atom, and therefore no fluorescence will occur. Repeating the whole experiment $n_{\text{exp}} \gg 1$ times, one can determine a superposition between $|0\rangle$ and $|1\rangle$, by measuring the number of excited states $n_{|1\rangle} \leq n_{\text{exp}}$ and calculating a mean excitation $p_m = n_{|1\rangle}/n_{\text{exp}}$.

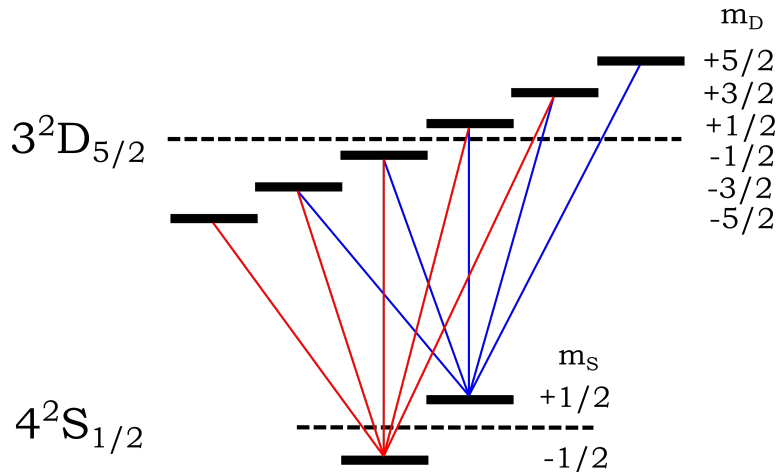


Figure 2.2.2: Zeeman sub-levels in $^{40}\text{Ca}^+$. A magnetic field strength $B \neq 0$ at the position of the ions leads to a Zeeman splitting. This detuning from the unperturbed center frequency (dashed lines) depends on the magnetic field strength, as well as the projections m_j (S) and m_j (D) of the total angular momentum quantum number of the respective state. Indicated in red and blue are the optical transitions between the Zeeman sub-levels, that can be addressed with a laser system operating at a wavelength of 729 nm. For the sake of simplicity, transitions that have a coupling strength to said light field that leads to too low photon scattering rates to be imaged by the EMCCD camera are omitted, as these transitions are not relevant within the scope of this thesis.

2.3 Light-Atom Interaction

Quantum gate operations can be realized by driving the qubit transition in a controlled way [19]. This can be achieved using a Titanium-Sapphire laser system operating at a wavelength of 729 nm. An acousto-optic modulator (AOM) that is installed in a double pass setup in the light path of said laser system precisely tunes the light field to the transition frequencies. Following the treatment of reference [30], the interaction between a traveling wave of a single mode laser and a harmonically trapped $^{40}\text{Ca}^+$ ion is discussed. We assume an effective two-level system, with the laser operating at a frequency close to the transition frequency. As the ion is trapped in a harmonic potential, its potential energy is quantized and can be described using the creation and annihilation operators a^\dagger and a , resulting in the Hamiltonian [30]

$$H_0 = \hbar\omega \left(a^\dagger a + \frac{1}{2} \right) + \frac{1}{2} \hbar\nu \sigma_z$$

with the reduced Planck constant \hbar , the trap frequency ω , the transition frequency ν , and the Pauli spin matrix σ_z . With the ladder operators σ^\pm , the interaction between the ion and the light field is given by [30]

$$H_1 = \frac{1}{2} \hbar\Omega \left(e^{i\eta(a+a^\dagger)} \sigma^+ e^{-i\nu_L t} + e^{-i\eta(a+a^\dagger)} \sigma^- e^{i\nu_L t} \right)$$

with Ω being the coupling constant, ν_L the frequency of the light, t the duration of the interaction, and η the Lamb-Dicke parameter being given by [30]

$$\eta = k\sqrt{\frac{\hbar}{2m\omega}}$$

where k is the wave number of the traveling wave, and m the mass of the ion. This leads to a total Hamiltonian

$$H = H_0 + H_1$$

which can be written in the interaction picture [31], using $H_I = U^\dagger H U$ with $U = e^{iH_0 t/\hbar}$, resulting in [30]

$$H_I = \frac{1}{2}\hbar\Omega \left(e^{i\eta(\hat{a}+\hat{a}^\dagger)}\sigma^+ e^{-i\Delta t} + e^{-i\eta(\hat{a}+\hat{a}^\dagger)}\sigma^- e^{i\Delta t} \right) \quad (2.3.1)$$

with $\hat{a} = ae^{i\omega t}$ and the detuning $\Delta = \nu_L - \nu$. Thereby, the rotating wave approximation (RWA) has been used, neglecting fast oscillating terms with $\exp(\pm i(\nu_L + \nu)t)$, which is valid for small detunings, as in this case the neglected terms correspond to fast oscillations that average out to zero over the time scales of interest [14]. In the Lamb-Dicke regime, being defined by $\eta^2(2n+1) \ll 1$, with n being the vibrational quantum number, equation (2.3.1) can be simplified further. For resonant carrier transitions, that do not change the vibrational state of the ion, the interaction Hamiltonian can be reduced to [30]

$$H_I = \frac{1}{2}\hbar\Omega_{n,n} (\sigma^+ + \sigma^-) \quad (2.3.2)$$

with $\Omega_{n,n} = \Omega(1 - \eta^2 n)$. Red side-band transitions, reducing the vibrational quantum number by one are described by [30]

$$H_I = \frac{1}{2}i\hbar\Omega_{n-1,n} (\hat{a}\sigma^+ - \hat{a}^\dagger\sigma^-) \quad (2.3.3)$$

with $\Omega_{n-1,n} = \Omega\eta\sqrt{n}$, and blue side-band transitions increasing the vibrational quantum number by one are described by [30]

$$H_I = \frac{1}{2}i\hbar\Omega_{n+1,n} (\hat{a}^\dagger\sigma^+ - \hat{a}\sigma^-) \quad (2.3.4)$$

with $\Omega_{n+1,n} = \Omega\eta\sqrt{n+1}$. The Hamiltonian given by equation (2.3.3) corresponds to the Jaynes-Cummings (JC) Hamiltonian [32], whereas the one given by equation (2.3.4) is referred to as anti-JC Hamiltonian. The coupling constant Ω is also known as Rabi frequency and for the given case of a quadrupole-allowed transition, can be estimated by [30]

$$\Omega \approx \frac{kE_0}{2\hbar}ea_0^2 \quad (2.3.5)$$

where k is the wave number, E_0 the electric field amplitude, e the elementary charge and a_0 the Bohr radius.

As stated above, side-band transitions change the vibrational quantum number. Depending on the number of ions loaded in the trap, the number of available modes of motion changes. In three dimensions, N trapped ions lead to $3 \cdot N$ modes of motion,

all of which are featuring red and blue side-band transitions. If for example two ions are loaded in the given linear Paul trap, there are two modes of motion in either of the three spacial dimensions. If the ions move collectively, either along the axial z-axis defined by the trap architecture, or one of the two radial dimensions x or y, the center of mass oscillates. This is called the center of mass, or common mode in axial or radial direction respectively. An oscillation along the axial direction that does not change the center of mass is called stretch mode. The equivalent to the axial stretch mode in the radial directions is called rocking mode. As the laser beam used for the spectroscopic experiments of this thesis propagates (except for a narrow angle) along the ion crystal's axis, to irradiate all trapped ions at once, the radial side-band transitions are suppressed with respect to the axial ones.

Side-band transitions play a vital part in the implementation of entangling operations between different physical qubits as is described in reference [33]. The red side-band transitions can be used to perform side-band cooling, which is explained in detail in reference [30].

Unitary operations U can be expressed as combinations between the Pauli matrices

$$\sigma_0 = \begin{pmatrix} 1 & 0 \\ 0 & 1 \end{pmatrix}, \sigma_x = \begin{pmatrix} 0 & 1 \\ 1 & 0 \end{pmatrix}, \sigma_y = \begin{pmatrix} 0 & -i \\ i & 0 \end{pmatrix}, \sigma_z = \begin{pmatrix} 1 & 0 \\ 0 & -1 \end{pmatrix},$$

as is shown in reference [34]. Any unitary operation can be interpreted as arbitrary rotation of the qubit on the Bloch sphere, as [34]

$$U = e^{i\Phi} \cdot \left(\cos\left(\frac{\theta}{2}\right) \cdot \sigma_0 - i \cdot \sin\left(\frac{\theta}{2}\right) \cdot (n_x \sigma_x + n_y \sigma_y + n_z \sigma_z) \right) \quad (2.3.6)$$

with Φ representing a global phase that is accumulated by applying the operation, and the unit vector

$$\mathbf{n} = \begin{pmatrix} n_x \\ n_y \\ n_z \end{pmatrix}$$

defining the rotation axis. When shining a resonant light pulse onto an ion, the resulting \mathbf{n} is perpendicular to the z-axis of the Bloch sphere, leading to the operation [34]

$$U_\varphi(\theta) = \exp\left(-i \cdot \frac{\theta}{2} \cdot (\sigma_x \cdot \cos(\varphi) + \sigma_y \cdot \sin(\varphi))\right) \quad (2.3.7)$$

with φ depending on the phase of the light field and $\theta = \Omega \cdot t$ depending on the duration of the light pulse t and the coupling strength Ω as approximated in equation (2.3.5). A bit-flip of a qubit corresponds to applying the operator $U_0(\pi)$ to it, which is implemented by shining a resonant light pulse of duration $\tau_\pi = \pi/\Omega$ onto the ion. Such a pulse is referred to as π -pulse, with τ_π also being called the π -time as the corresponding rotation angle θ is given by $\Omega \cdot \tau_\pi = \pi$.

2.4 Rabi Spectroscopy

In the discussion on unitary operations, the detuning $\Delta = \nu_L - \nu$ between the laser frequency ν_L and the transition frequency ν is assumed to be zero. This assumption

has to be lifted as a detuning of zero cannot feasibly be produced under real world conditions. However, for typical experiments one can still assume $\Delta \ll \omega$, with ω being the trap frequency.

Investigating the interaction of a detuned light field and a trapped ion by solving the corresponding time-dependent Schrödinger equation $i\hbar\partial_t\Psi = H\Psi$, the interaction Hamiltonian given by equation (2.3.1) is used as a starting point. Necessary assumptions to simplify the calculations are:

- the assumption of the Lamb-Dicke regime $\eta^2(2n+1) \ll 1$
- a sufficiently low laser intensity leading to $\Omega \ll \omega$
- neglecting the motion of the ion and thus neglecting the modulation of the laser frequency with the trap frequency in the rest frame of the ion
- assuming an effective two level system neglecting the influence of other levels
- restricting the investigation to carrier transitions.

With these assumptions in mind, the ansatz $\Psi = c\Psi_1 + d\Psi_2$ can be inserted in the time dependent Schrödinger equation, leading to the set of coupled differential equations [30]

$$i \begin{pmatrix} \dot{c} \\ \dot{d} \end{pmatrix} = \frac{\Omega}{2} \cdot \begin{pmatrix} 0 & e^{i\Delta t} \\ e^{-i\Delta t} & 0 \end{pmatrix} \begin{pmatrix} c \\ d \end{pmatrix}. \quad (2.4.1)$$

Introducing the coefficients $\tilde{c} = c \cdot \exp(-i\Delta t/2)$ and $\tilde{d} = d \cdot \exp(i\Delta t/2)$, a coordinate transformation is used to simplify equation (2.4.1) to

$$i \begin{pmatrix} \dot{\tilde{c}} \\ \dot{\tilde{d}} \end{pmatrix} = \frac{1}{2} \begin{pmatrix} \Delta & \Omega \\ \Omega & -\Delta \end{pmatrix} \begin{pmatrix} \tilde{c} \\ \tilde{d} \end{pmatrix} \quad (2.4.2)$$

which can be solved by calculating the corresponding eigenvalues $\lambda_{1,2} = \pm i\tilde{\Omega}/2$ and eigenvectors

$$v_{\lambda_1} = A \begin{pmatrix} -\Omega \\ \tilde{\Omega} + \Delta \end{pmatrix}, \quad v_{\lambda_2} = B \begin{pmatrix} \tilde{\Omega} + \Delta \\ \Omega \end{pmatrix} \quad (2.4.3)$$

where $\tilde{\Omega} = \sqrt{\Omega^2 + \Delta^2}$ is the effective Rabi frequency. This gives the solution

$$\begin{pmatrix} \tilde{c} \\ \tilde{d} \end{pmatrix} = v_{\lambda_1} e^{\lambda_1 t} + v_{\lambda_2} e^{\lambda_2 t} \quad (2.4.4)$$

that can further be simplified to

$$\begin{pmatrix} \tilde{c} \\ \tilde{d} \end{pmatrix} = \begin{pmatrix} A_1 \\ A_2 \end{pmatrix} \cdot \cos\left(\frac{\tilde{\Omega}t}{2}\right) + \begin{pmatrix} B_1 \\ B_2 \end{pmatrix} \cdot \sin\left(\frac{\tilde{\Omega}t}{2}\right) \quad (2.4.5)$$

where the coefficients $A_{1,2}$ and $B_{1,2}$ can be determined by the initial conditions of the system. For a system that is initially in the ground state Ψ_1 , the probability amplitudes $p_{1,2}$ are given by [35]

$$p_1 = |\tilde{c}|^2 = \left| \frac{\Omega}{\tilde{\Omega}} \right|^2 \cdot \sin^2\left(\frac{\tilde{\Omega}t}{2}\right) \quad (2.4.6)$$

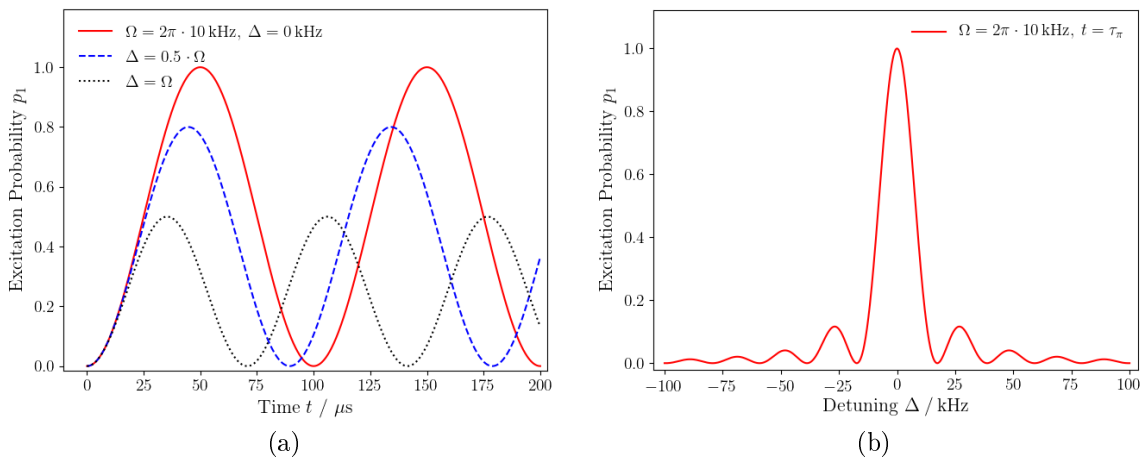


Figure 2.4.1: Excitation probability p_1 for a light pulse as described with equation (2.4.6). (a) A variation of the light pulse duration leads to Rabi oscillations with excitation probability maxima at multiples of the π -time. (b) Equation (2.4.6) shows a global maximum for a π -time pulse duration and zero detuning between the laser frequency and transition frequency.

$$p_2 = \left| \tilde{d} \right|^2 = 1 - p_1 \quad (2.4.7)$$

which leads to Rabi oscillations [36] as shown in figure 2.4.1a. As visualized in figure 2.4.1b, the excitation probability p_1 reaches its maximum if the laser frequency is equal to the transition frequency ($\Delta = 0$), and the light pulse duration is equal to multiples of the π -time.

2.5 Ramsey Spectroscopy

A sequence of quantum gate operations that is of major significance is the so called Ramsey sequence, named after N. F. Ramsey [37]. The Ramsey sequence consists of two $\pi/2$ -pulses $U_\varphi(\pi/2)$ with a waiting time τ between them. Assuming resonant light pulses, starting with a qubit in the ground state $|\psi\rangle = |0\rangle$, two $\pi/2$ -pulses with no phase offset between them result in

$$U_\varphi\left(\frac{\pi}{2}\right) U_\varphi\left(\frac{\pi}{2}\right) |\psi\rangle = U_\varphi(\pi) |0\rangle = |1\rangle .$$

In the non-resonant case¹ ($\Delta \neq 0$) the probability to excite an ion from the ground state $4^2S_{1/2}$ ($m_j(S) = -1/2$) to the excited state $3^2D_{5/2}$ ($m_j(D) = -1/2$), by applying

¹using the same assumptions as listed in section 2.4

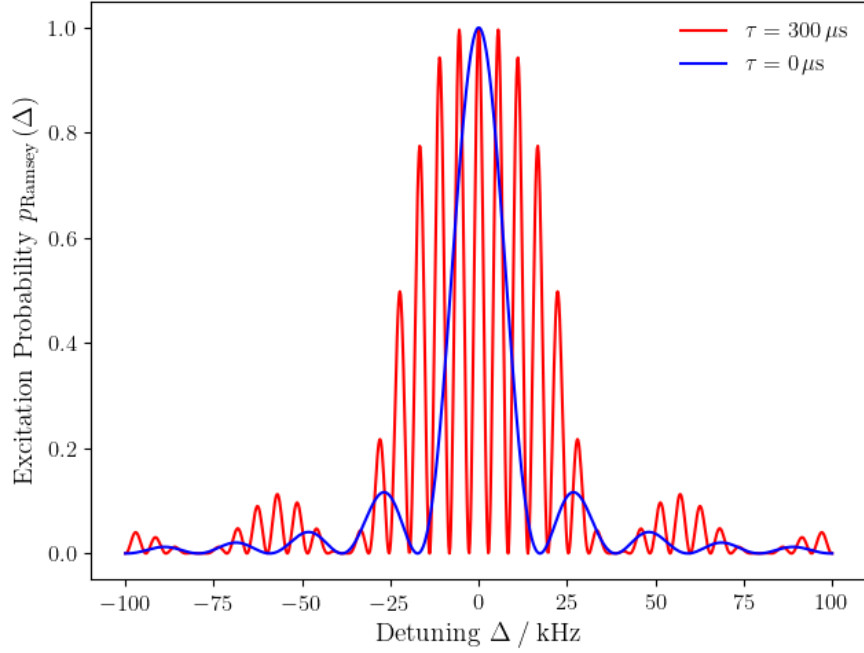


Figure 2.5.1: Excitation probability after a Ramsey sequence. The simulated Ramsey sequence is performed with a Rabi frequency of $\Omega = 2\pi \cdot 10$ kHz and a waiting time of $\tau \in \{0, 300\}$ μ s.

a Ramsey sequence to it is given by [26]²

$$p_{\text{Ramsey}}(\Delta) = \frac{4\Omega^2}{\tilde{\Omega}^2} \cdot \sin^2\left(\frac{1}{2}\tilde{\Omega}\tau_{\pi/2}\right) \cdot \left[\cos\left(\frac{1}{2}\tilde{\Omega}\tau_{\pi/2}\right) \cdot \cos\left(\frac{1}{2}\Delta\tau + \frac{1}{2}\varphi\right) - \frac{\Delta}{\tilde{\Omega}} \cdot \sin\left(\frac{1}{2}\tilde{\Omega}\tau_{\pi/2}\right) \cdot \sin\left(\frac{1}{2}\Delta\tau + \frac{1}{2}\varphi\right) \right]^2 \quad (2.5.1)$$

with the effective Rabi frequency $\tilde{\Omega} = \sqrt{\Omega^2 + \Delta^2}$, and the $\pi/2$ -time $\tau_{\pi/2} = 0.5 \cdot \tau_{\pi}$, resulting in the spectrum shown in figure 2.5.1. Setting the waiting time between the $\pi/2$ -pulses as well as the phase offset between them to zero is equivalent to applying a π -pulse, and therefore leads to an equivalent situation as discussed in section 2.4.

Assuming a detuning Δ close to resonance ($\Delta \ll \Omega$) as well as the first $\pi/2$ -pulse $U_0(\pi/2)$ having a phase of zero, the Ramsey sequence is investigated on the Bloch sphere as shown in figure 2.5.2. The first light pulse brings the qubit from the ground state $|0\rangle$ to the equatorial x-y-plane (see figure 2.5.2a). During the waiting time τ , the state of the qubit can be interpreted as rotating around z-axis of the Bloch sphere (see figure 2.5.2b), where the rotation angle φ is given by [26]

$$\varphi = \Delta \cdot \tau. \quad (2.5.2)$$

In order to excite the qubit from the equatorial plane to the excited state $|1\rangle$, the second $\pi/2$ -pulse $U_{\varphi}(\pi/2)$ has to have a phase offset of φ with respect to the first pulse (see figure 2.5.2c).

²Note that the definition of the phase φ in equation (2.5.1) differs by a factor of two with respect to reference [26].

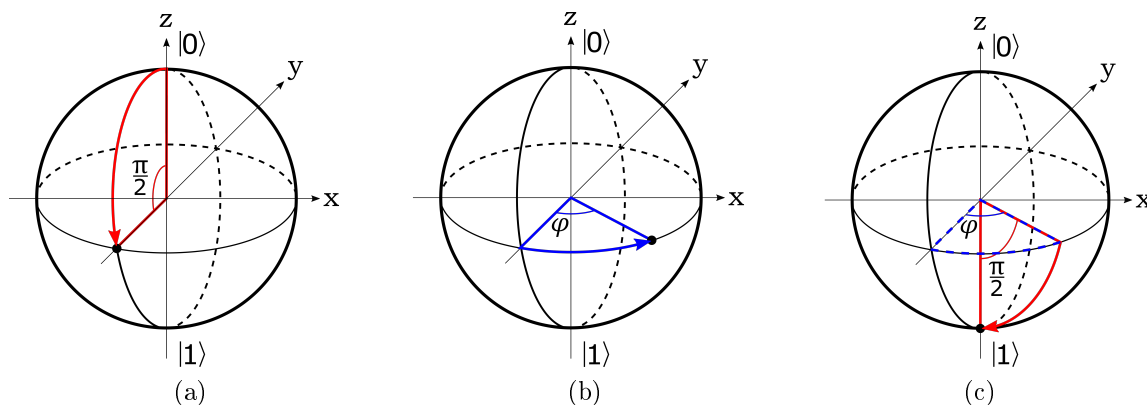


Figure 2.5.2: The Ramsey sequence visualized on a Bloch sphere with the laser frequency being close to the transition frequency ($\Delta \ll \Omega$). (a) The first $\pi/2$ -pulse brings the qubit from its initial state $|0\rangle$ to the x-y-plane. (b) During the waiting time τ , the population performs a rotation around the z-axis, with the rotation angle φ being given by equation (2.5.2). (c) With a phase offset of φ with respect to the first pulse, the second $\pi/2$ -pulse brings the qubit to its excited state $|1\rangle$.

Investigating the Ramsey sequence further, it has to be noted that the waiting time τ cannot be increased infinitely as several noise processes lead to an evolution of the state after the first $\pi/2$ -pulse that differs from the discussion above. Due to amplitude damping, a state $|\psi\rangle = \alpha|0\rangle + \beta \cdot e^{i\varphi}|1\rangle$ can with some probability decay to the ground state $|0\rangle$. This process is related to the operator $U_\varphi(\pi/2)$, as well as to a relaxation time T_1 . Intuitively, amplitude damping is limiting the waiting time as the excited state $|1\rangle$ has a finite lifetime. Another important noise process is called phase damping, where partial information about the phase φ is lost [11]. Phase damping can occur as a result of perturbation and is related to the operator $S_z(\varphi)$ and the phase coherence time T_2 [11]. As in the experimental setup $T_2 \ll T_1$ is given, phase damping dominates, and the resulting excitation probability p_{Ramsey, T_2} exponentially approaches a value of $p_{\text{Ramsey}, T_2} \rightarrow 0.5$ for $\tau \rightarrow \infty$ [38], which can be modeled as

$$p_{\text{Ramsey}, T_2}(\Delta) = \frac{1}{2} + \left(p_{\text{Ramsey}}(\Delta) - \frac{1}{2} \right) \cdot e^{-\frac{\tau}{T_2}}. \quad (2.5.3)$$

Chapter 3

Frequency Stabilization

With the equations (2.4.6) and (2.5.3) in mind, in order to perform a $U_0(\pi)$ operation, a resonant π -pulse is required. Thus, the used laser system has to be accurately tuned to the corresponding transition frequencies, as well as frequency stable with respect to them over the measurement time. Therefore, section 3.1 discusses how a laser system can be stabilized, with the aid of a stable reference frequency, focusing on how to use atomic clock experiments as a source of reference. Furthermore, section 3.1 introduces the Allan deviation [39] to quantify the stability of a frequency source.

Section 3.2 discusses how Rabi spectroscopy can be implemented in the experimental setup in order to stabilize the frequency of the laser system driving the qubit transition. Section 3.3 concludes this chapter, discussing the implementation of Ramsey spectroscopy to frequency stabilize a laser system, motivating the major pitfalls that are encountered using this approach. A way to circumvent these pitfalls will be presented in the next chapter.

3.1 Stable References

Frequency stabilization of lasers is in general achieved utilizing a stable reference frequency to which the laser system can be stabilized to. Sources for such a reference frequency can be e.g. high-finesse cavities, or atomic clock transitions. In a previous master's thesis by Roman Stricker [40], the installed laser system has been stabilized to an optical high-finesse cavity using the Pound-Drever-Hall technique [41]. The resulting spectral line width has been measured as 3.4 (4) Hz at 4s averaging time [40]. Frequency instabilities have been measured to be below 1 Hz at averaging times between 1 s and 100 s [40]. Over the course of multiple minutes however, the cavity is unstable. In a similar system, a long term drift of 0.37 Hz/s has been measured over a period of one month [42]. Furthermore, the magnetic field strength at the position of the trapped ions is not constant, introducing undesired Zeeman shifts on the qubit transition.¹ As the laser system has to be stable with respect to the qubit transition, these shifts have to be accounted for. One goal of this thesis is to improve upon the

¹The residual magnetic field strength thereby most likely stems from irregularities in the current of the magnetic field coils generating the desired Zeeman shifts, or from magnetic fields generated by e.g. neighboring experiments or electronics inside the laboratory.

already installed frequency stabilization, using precision spectroscopy to measure and correct these drifts and offsets in an automated manner.

Atomic transitions can be used as a stable reference frequency source for a laser system. For this, the transition frequency is compared to the laser frequency. The laser system is then stabilized by keeping the detuning between these frequencies constant. The transition frequency ν can be converted to a time interval $\tau = 1/\nu$ between ticks of an atomic clock. The stability of an atomic clock, and thereby also the stability of the laser system stabilized by the clock, can be characterized with the Allan deviation [39]. Following the treatment of reference [43], the Allan deviation can be motivated by assuming that the clock under test is compared to a reference clock which is assumed to be perfectly stable. At each tick of the reference clock, separated by a time interval τ , the time difference x_k between the two clocks is measured. The index k thereby indicates the k -th tick of the reference clock. The average frequency of the clock under test can then be estimated as [43]

$$y_k = \frac{x_k - x_{k-1}}{\tau}.$$

The frequency difference between consecutive comparisons is given by [43]

$$y_{k+1} - y_k = \frac{x_{k+1} - 2x_k + x_{k-1}}{\tau} \quad (3.1.1)$$

which is an estimator for the stability of the clock under test. Assuming that the root-mean-square (RMS) of equation (3.1.1) has a well-defined value i.e. equation (3.1.1) does not systematically depend on the index k , the two-sample Allan variance σ_y^2 is the normalized mean square value of $y_{k+1} - y_k$, estimated over all possible values of k , and given by [43]

$$\sigma_y^2(\tau) = \frac{1}{2(N-2)\tau^2} \sum_{k=2}^{N-1} (x_{k+1} - 2x_k + x_{k-1})^2 \quad (3.1.2)$$

with N being the number of comparisons. The square root of σ_y^2 gives the Allan deviation σ_y which can then be used as a measure of frequency stability. In order to familiarize with the achievable stability in trapped ion experiments, Allan deviations of e.g. $5 \cdot 10^{-15}/\sqrt{\tau(s)}$ [44] or $1.4 \cdot 10^{-16}/\sqrt{\tau(s)}$ [45] have been demonstrated.

In the given experimental setup, precision spectroscopy can be performed on all $4^2S_{1/2}$ to $3^2D_{5/2}$ Zeeman sub-level transitions introduced in section 2.2, using the laser system driving the qubit transition [26]. In order to stabilize the laser frequency, the transitions $(-1/2, -1/2)$ and $(-1/2, -5/2)$ are chosen, as the first is the qubit transition and the second has a stronger sensitivity to the magnetic field.² The frequency of the chosen transitions is given by

$$\nu_i = \nu_{\text{center}} + \Delta\nu_Z(m_j(D^{(i)}), g_D) - \Delta\nu_Z(m_j(S^{(i)}), g_S) \quad (3.1.3)$$

²In theory any pair of transitions depicted in figure 2.2.2 can be selected for the discussion in this section, provided they show different magnetic sensitivities. The choice of $(-1/2, -1/2)$ and $(-1/2, -5/2)$ is a pragmatic one as the experimental setup has to be calibrated for the $(-1/2, -1/2)$ transition to perform quantum gate operations.

where $i \in \{1, 2\}$ is used as an abbreviated label for the transitions $(-1/2, -1/2)$ and $(-1/2, -5/2)$, ν_{center} is the unperturbed $4^2\text{S}_{1/2}$ to $3^2\text{D}_{5/2}$ center frequency, and $\Delta\nu_Z$ is the Zeeman shift corresponding to the respective projection $m_j(L^{(i)})$ of the total angular momentum of the corresponding transition's state $L \in \{\text{S}, \text{D}\}$. As the transitions have a different sensitivity to magnetic field, the system of equations

$$\begin{pmatrix} \nu_1 \\ \nu_2 \end{pmatrix} = \nu_{\text{center}} - \frac{\mu_B \cdot B}{\hbar} \cdot \left(g_S \cdot \begin{pmatrix} m_j(\text{S}^{(1)}) \\ m_j(\text{S}^{(2)}) \end{pmatrix} - g_D \cdot \begin{pmatrix} m_j(\text{D}^{(1)}) \\ m_j(\text{D}^{(2)}) \end{pmatrix} \right) \quad (3.1.4)$$

can be solved for ν_{center} and the magnetic field strength B . Intuitively, the center frequency ν_{center} changes if the transition frequencies ν_1 and ν_2 are changed equally over time, and the magnetic field strength B changes if ν_1 and ν_2 are changed with respect to one another. This way, the drifts and offsets between the transition frequencies and laser frequency can be measured and thus also compensated for independently. After accumulating some measurement results for ν_{center} and B , a linear regression can be performed, yielding an estimate of the current drift rates $\dot{\nu}_{\text{center}}$ and \dot{B} . The current values for ν_{center} and B can then be extrapolated from the previous measurements using

$$\nu_{\text{center}}(t) = \nu_{\text{center}}(t_0) + (t - t_0) \cdot \dot{\nu}_{\text{center}} \quad (3.1.5)$$

and

$$B(t) = B(t_0) + (t - t_0) \cdot \dot{B} \quad (3.1.6)$$

with t being the current time, and t_0 the time of the latest measurement. This way, the current value of every $4^2\text{S}_{1/2}$ to $3^2\text{D}_{5/2}$ Zeeman sub-level transition frequency can be estimated using equation (3.1.4). As the light field can be accurately tuned to the desired transition frequency, it is possible to cancel out the undesired drifts and offsets. In order to automate all tasks mentioned above, a computer program has been written that performs them periodically and thereby continuously re-calibrates the laser frequency.

3.2 Rabi Spectroscopy

As introduced in section 2.4, when ground state ions interact with single light pulses of a given duration, the excitation probability is maximized, if the laser frequency is equal to a transition frequency and the pulse duration corresponds to the π -time. Therefore, the idea of Rabi spectroscopy [46], as it is implemented in the experimental setup, is to sample the excitation spectrum in order to determine this maximum. Once the resonances assigned to the transitions $(-1/2, -1/2)$ and $(-1/2, -5/2)$ are measured, frequency stabilization as described in section 3.1 can be performed.

In order to assign and measure these resonances, prior knowledge on the transition frequencies is required. Therefore, a mean excitation spectrum over a broad frequency range is measured, which can be found in figure 3.2.1. The shown spectrum is taken from two trapped $^{40}\text{Ca}^+$ ions, sweeping the input frequency of the double-pass AOM from 223 MHz to 247 MHz in steps of 1 kHz.³ Every mean excitation data point is thereby the result of one hundred experiments, with every experiment consisting of

³The actual detuning of the light field frequency is twice the input frequency to the AOM.

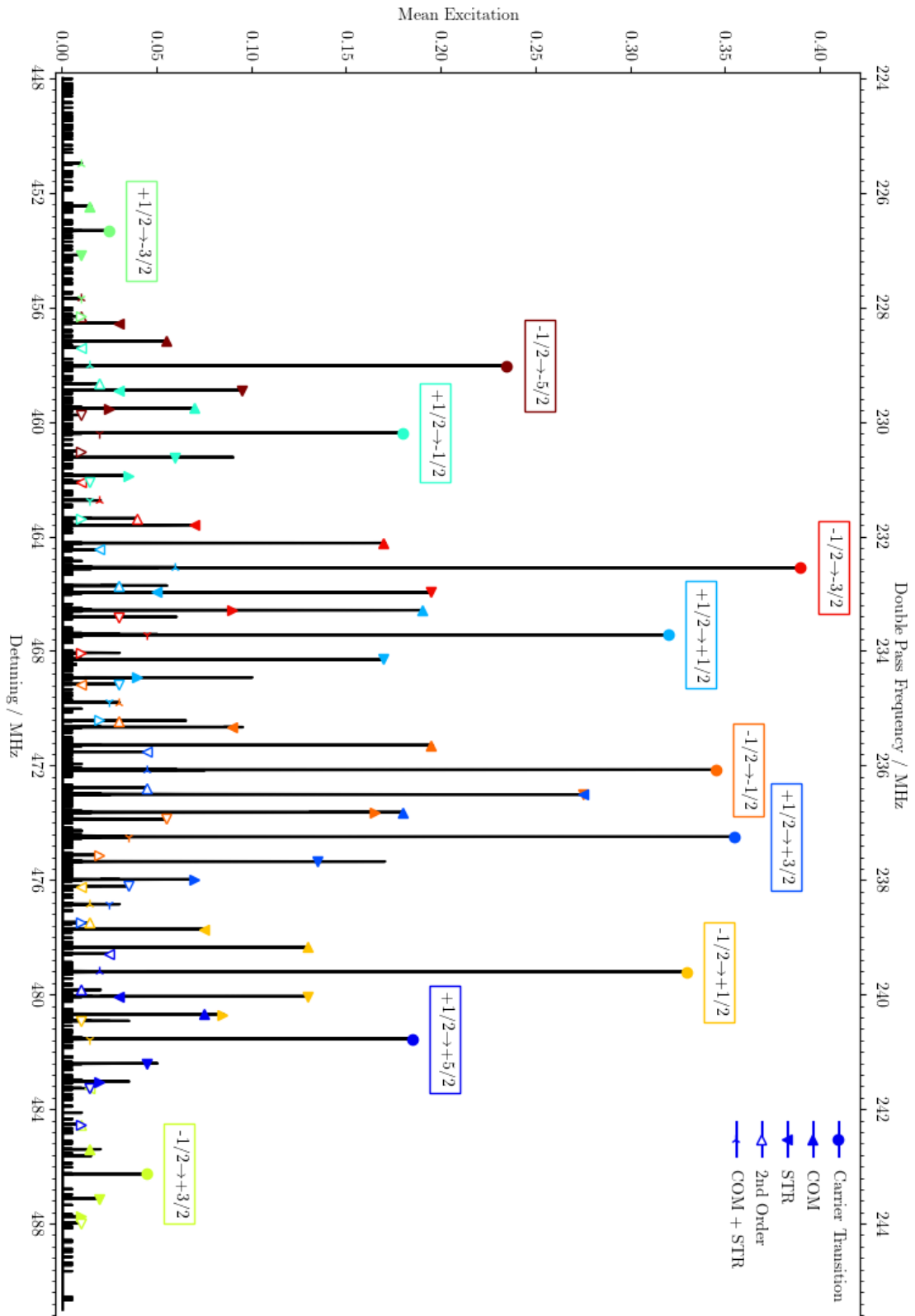


Figure 3.2.1: Spectrum of the $4^2S_{1/2}$ to $3^2D_{5/2}$ transition as discussed in section 3.2. The labels COM and STR are used for the ion crystal's axial common and stretch modes respectively. Side-band transitions are marked with the same color as their corresponding carrier transition.

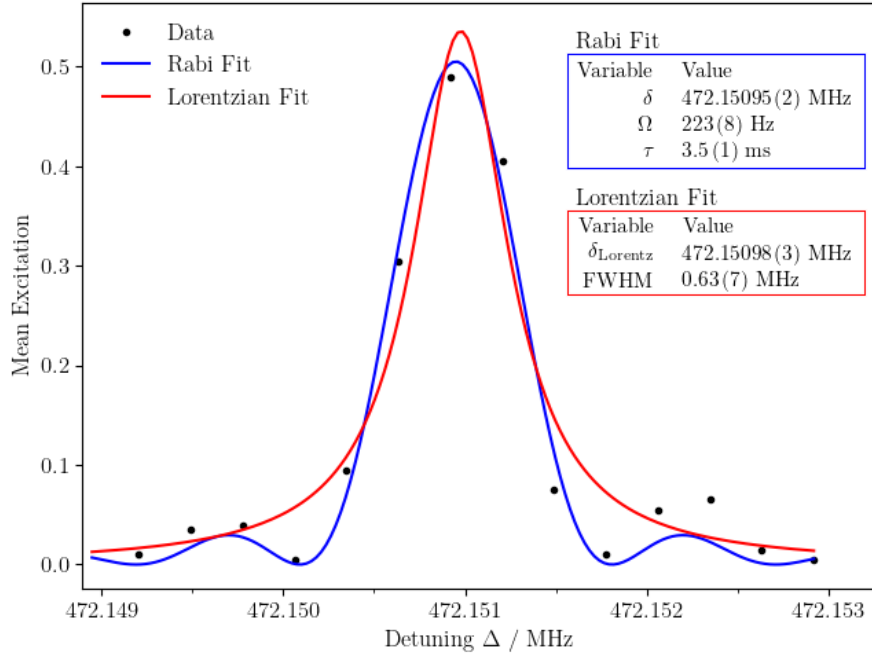


Figure 3.2.2: Mean excitation of the $(-1/2, -1/2)$ transition, as described in section 3.2. The blue line labeled *Rabi Fit* corresponds to a least squares fit with equation (2.4.6) as model function. The corresponding fit parameters are listed inside the blue box. The variables δ_{Lorentz} and FWHM correspond to the location of the maximum and the full width half maximum of the shown *Lorentzian Fit* (red line and box).

Doppler cooling [21], followed by a light pulse with a pulse duration of 100 μs , concluding with state detection via electron shelving [29]. All transitions shown in figure 2.2.2 are assigned to resonances in figure 3.2.1, including their axial side-bands⁴, sufficiently reducing the uncertainty of their detuning with respect to the laser frequency to a few Kilohertz.

Performing such an initial measurement is time consuming, as the data shown in figure 3.2.1 consists of more than $2.4 \cdot 10^4$ data points, and the generation of a single data point takes about one second. However, a broad spectrum as the shown one is only required, if the available prior knowledge on the transition frequencies is not sufficient to assume $\Delta \ll \omega$, as required by the discussion of section 2.4. Once a broad spectrum has been measured, the laser system can be continuously re-calibrated to the transition frequencies as discussed in section 3.1.

With the uncertainty of the detuning reduced to a few Kilohertz, it is possible to sample the spectrum around a single transition frequency. Measuring the spectrum around the $(-1/2, -1/2)$ transition frequency using 14 data points that are equally spaced over an approximately 4 kHz wide frequency range using a pulse duration of about 3.5ms, leads to a graph as shown in figure 3.2.2. The number of measured data points is thereby a trade-off between the measurement time and having enough resolution to confidently analyze the data. A least squares fit of the data estimates the detuning between the transition frequency and the laser frequency. The excitation

⁴As the laser beam is propagating along the trap axis (except for a narrow angle), the radial side-bands are suppressed and cannot be assigned to maxima with the given signal-to-noise ratio.

probability after a single pulse can be modeled with equation (2.4.6). However, a simplified model function like e.g. a Lorentzian function yields similar results, as can be seen by comparing the fits shown in figure 3.2.2. The detuning $\delta = 472.15095$ (2) MHz determined by the fit using equation (2.4.6) is thereby within one standard deviation of the detuning $\delta_{\text{Lorentz}} = 472.15098$ (3) MHz determined by the Lorentzian fit. Therefore, the Lorentzian fit is chosen over the other when automating Rabi spectroscopy in order to keep the number of parameters of the computer program low.

Concerning the choice of the pulse duration, there are a few things to keep in mind. First of all, equation (2.4.6) can be interpreted as a Fourier transformation of the rectangular light pulse in the time domain [14]. Therefore, the spread of the resulting spectrum and the pulse duration are inversely proportional. Secondly, an unfortunate choice of the pulse duration can lead to a splitting of the main peak, as for a pulse duration τ_0 with e.g. $\tau_\pi < \tau_0 < 3 \cdot \tau_\pi$, the resulting rotation angle on the Bloch sphere is between 180° and 540° . This effect can be accounted for, however unnecessarily complicates the data analysis. By either reducing the Rabi frequency and therefore increasing the π -time such that $\tau_\pi \geq \tau_0$, or by increasing the pulse duration drastically such that $T_2 \ll \tau_0$ the splitting can be avoided. The latter solution thereby exploits the fact, that due to the relaxation time T_1 and the phase coherence time T_2 the Rabi oscillations exponentially approach a excitation probability of 0.5, similarly to the Ramsey excitation given by equation (2.5.3).

3.3 Ramsey Spectroscopy

Ramsey spectroscopy [37] as described in section 2.5 can be implemented similarly to how the Rabi spectroscopy is implemented in section 3.2. For a phase offset of $\varphi = 0$ between the $\pi/2$ -pulses of the Ramsey sequence, the excitation probability as given with equation (2.5.1) shows a maximum at zero detuning. Therefore, the mean excitation spectrum can again be sampled and the resulting Ramsey fringes (see figure 3.3.1a) can be analyzed with a least squares fitting algorithm. As shown in figure 3.3.1b, the number of Ramsey fringes is proportional to the waiting time of the Ramsey sequence and the location of the maxima is dependent on the phase offset between the $\pi/2$ -pulses. If the waiting time is chosen too large with respect to the sampled frequency range, the central fringes are ambiguous requiring additional prior knowledge on the transition frequency to thoroughly analyze the data.

Another possibility to implement Ramsey spectroscopy is given, if $\Delta \ll \Omega$ can be assumed. In this regime, it is sufficient to measure two mean excitation data points, with the measurements using a phase offset of $\varphi = \pm 90^\circ$ between the $\pi/2$ -pulses respectively. As shown in figure 3.3.2, if the detuning between the laser frequency and the central Ramsey fringe maximum is zero, the mean excitation data points have a value of 0.5. If there is a non-zero detuning between laser frequency and Ramsey fringe maximum, the data points show a corresponding imbalance. As the central fringes are ambiguous for longer waiting times, the idea is to incrementally increase the knowledge of the transition frequency by incrementally increasing the waiting time and re-calibrating the laser system after each measurement. An implicit assumption of this scheme is that the laser frequency does not change by more than half the frequency range of a Ramsey fringe between measurements. If this assumption is not fulfilled, the

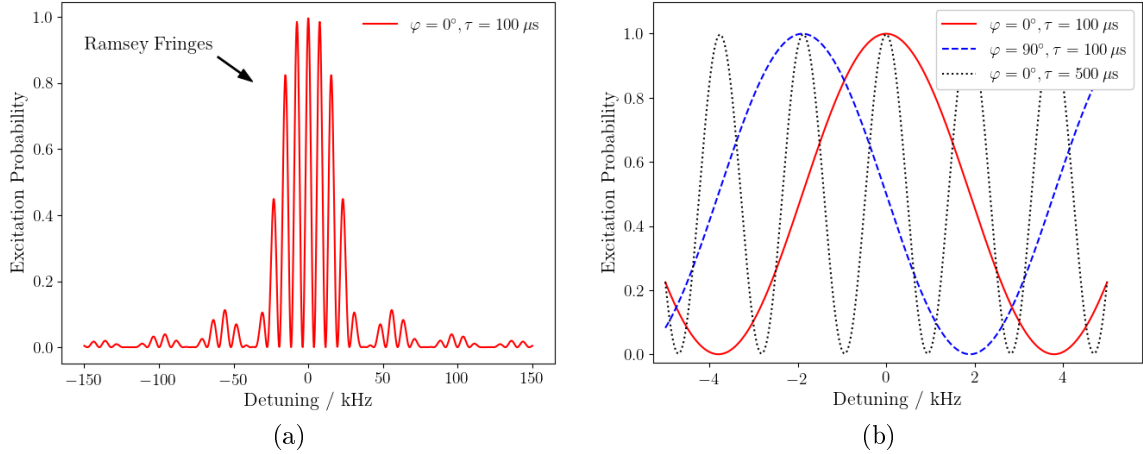


Figure 3.3.1: The excitation probability after a Ramsey sequence against the detuning between the applied $\pi/2$ -pulses and the qubit transition frequency, as described in section 3.3. (a) The overall profile shows, that the Ramsey sequence leads to several local maxima. These maxima are called Ramsey fringes. (b) A close-up with different values for the phase φ and waiting time τ of the Ramsey sequence shows, that the number of the fringes is proportional to τ , while the location of their maxima depends on φ .

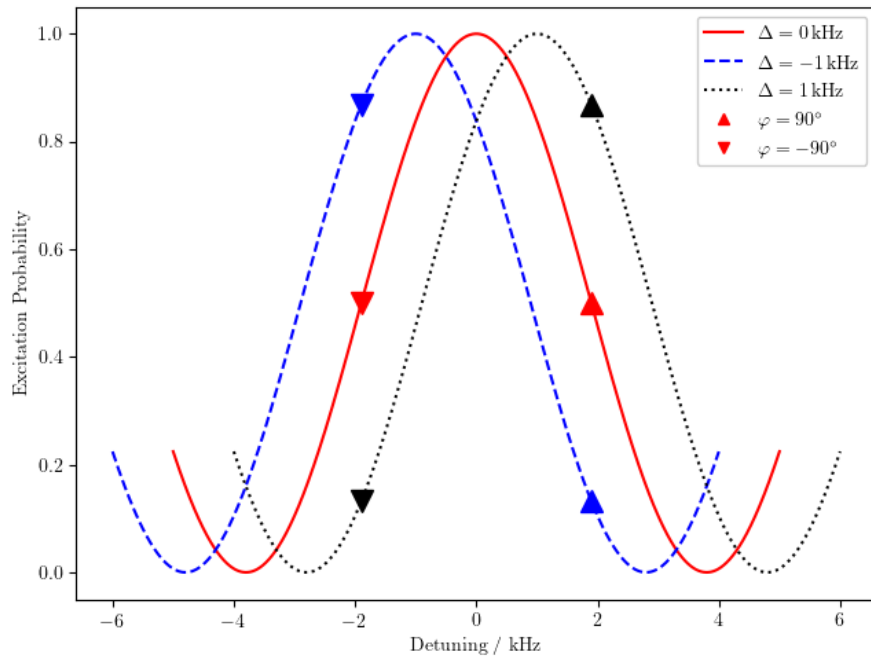


Figure 3.3.2: The excitation probability with a Ramsey sequence versus the detuning between the used laser system and the predicted transition frequency. Measuring two mean excitation data points with a phase offset of $\varphi = -90^\circ$ (triangle pointing down) and $\varphi = 90^\circ$ (triangle pointing up) respectively, the detuning Δ between the predicted and the true transition frequency can be deduced. If $\Delta = 0$ (red) the data points are balanced, while $\Delta \neq 0$ (blue and black) leads to a corresponding imbalance.

data analysis wrongfully assumes to measure the detuning from the central Ramsey fringe. This error in the data analysis is called fringe hopping, which leads to errors in the estimated detuning. Furthermore, it is clear that the choice of the waiting time is a trade-off between robustness with respect to fringe hopping and a better resolution. Therefore, the waiting time depends on the prior knowledge of the transition frequency and has to be chosen accordingly for each measurement. An algorithm that prevents fringe hopping and automatically calculates the optimal waiting time will be presented in the next chapter.

Chapter 4

Bayesian Inference

There are two main philosophies on how to statistically interpret measured data: Frequentism and Bayesianism [47]. Algorithms based on either one of them often yield similar results. However, depending on the given problem, one of the two approaches can lead to a more straight forward solution than the other.

Within section 4.1, the frequentist least squares method is discussed. In section 4.2, the Bayesian philosophy as well as practical Bayesian inference of Ramsey experiments is introduced. The chapter concludes with comparing the least squares method and Bayesian inference with each other, highlighting their advantages and disadvantages by using examples based on the experiment at hand, where the results of either approach differ. Furthermore, this shows how Bayesian inference produces a direct solution to fringe hopping and finding the optimal waiting time in Ramsey experiments.

4.1 Frequentism

Frequentist analysis links the occurrence frequency of a given event with its probability: The more frequent an event has been observed, the higher is its probability. In 1805 A. M. Legendre developed the method of least squares with this ansatz [48], followed with mathematical derivations and proofs by R. Adrain in 1808 [49], C. F. Gauss in 1809 [50], and P.-S. Laplace in 1810 [51].

In the following, the least squares method is motivated analogously to the proof by C. F. Gauss. Assume that after some experiment, $N \in \mathbb{N}$ data points have been measured. The underlying physical phenomenon creating the data is described by the function $\tilde{y}(x)$. For a parameter x_i , the probability to measure a value y_i is assumed to be given by a Gaussian distribution

$$P_{\text{Gauss}}(y_i; \tilde{y}(x_i), \sigma) = \frac{1}{\sqrt{2\pi\sigma^2}} \cdot \exp\left(-\frac{(y_i - \tilde{y}(x_i))^2}{2\sigma^2}\right) \quad (4.1.1)$$

where $\sigma \in \mathbb{R}^+$ is the standard deviation. Given a model function $y(\theta, x)$, where θ is a parameter vector that represents a set of parameters different from x , the goal is now to find the most probable parameter vector θ' , such that $y(\theta', x)$ best approximates $\tilde{y}(x)$, given the available data points (x_i, y_i) . This best approximation and therefore θ' can be found, when the distance ϵ between $y(\theta, x)$ and $\tilde{y}(x)$ is minimal. One possibility

to define ϵ is utilizing the squared differences between the data points and the model function

$$\epsilon = \sum_{i=1}^N (y_i - y(\theta, x_i))^2 . \quad (4.1.2)$$

Minimizing equation (4.1.2) yields the most probable parameter vector θ' .

The name least squares method is a result of this minimization as well, as the sum of the squared differences is minimized. Squaring the differences also leads to ϵ being differentiable, provided $y(\theta, x)$ is differentiable. Therefore, ϵ can in many practical cases be minimized by solving $d\epsilon/d\theta|_{\theta=\theta'} = 0$, if θ is one dimensional, or by solving $\nabla\epsilon(\theta)|_{\theta=\theta'} = \underline{0}$ in the multi dimensional case, with $\nabla\epsilon(\theta)$ being the gradient vector of ϵ , and $\underline{0}$ the zero vector.

4.2 Bayesianism

The main difference between Bayesianism and frequentism is the interpretation of probabilities. While a frequentist links probabilities to the occurrence frequency of an event, a Bayesianist refers to the probability as their knowledge about the underlying phenomenon creating these events. This difference leads to conclusions and methods that agree in many cases, but yield considerably different results in others [47]. The foundation of Bayesianism is a theorem, first formulated by T. Bayes and published in 1763 [52], two years after his death. A decade later, P.-S. Laplace independently comes up with Bayes' theorem and uses it as an axiom in 1774 [53]. In the following decades, P.-S. Laplace developed the theory around Bayes' theorem into its modern form:

The probability p of a hypothesis A given some evidence B is called the conditional probability $p(A|B)$. Bayes' theorem is represented by the equation [54]

$$p(A|B) = \frac{p(A) \cdot p(B|A)}{p(B)} \quad (4.2.1)$$

where $p(A)$ and $p(B)$ are the probability of the hypothesis and evidence respectively. In the case of a discrete set of available hypotheses A_i with $i \in \mathbb{N}$, equation (4.2.1) can be extended to

$$p(A|B) = \frac{p(A) \cdot p(B|A)}{\sum_i p(A_i) p(B|A_i)} \quad (4.2.2)$$

utilizing the law of total probability [55]

$$p(B) = \sum_i p(A_i) p(B|A_i) .$$

For a continuous parameter space η of available hypotheses, equation (4.2.1) can similarly be extended to

$$p(A|B) = \frac{p(A) \cdot p(B|A)}{\int_{\eta} p(A') p(B|A') dA'} . \quad (4.2.3)$$

Bayes' theorem can be explained with the help of the following simple scenario. A cat catches mice and brings them into the house. The cat's owner is interested in the probability that the cat has caught a mouse given that it is entering. In this

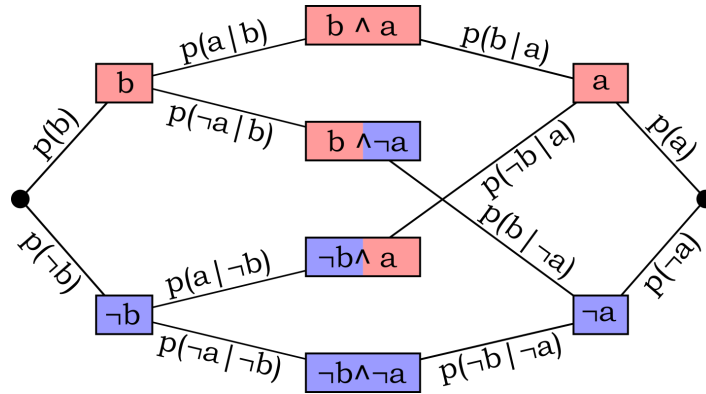


Figure 4.2.1: Conditional probability. This graph shows how the (conditional) probabilities of a scenario with two binary variables $A \in \{a, \neg a\}$ and $B \in \{b, \neg b\}$ link all possible states as described in section 4.2.

scenario there are two binary variables of interest. One of them states if the cat has caught a mouse a , or not $\neg a$, and the other one if it enters the house b , or not $\neg b$. The combination of these parameters can be labeled with the logical symbol \wedge , e.g. the cat is entering the house *and* has caught a mouse can be labeled as $b \wedge a$. The conditional probability the owner of the cat is interested in is then given by $p(a|b)$. All possible states as well as the probabilities linking them are depicted by the graph shown in figure 4.2.1. The probability that the cat enters the house *and* has caught a mouse $p(b \wedge a)$, can now be calculated from either side of the graph, as

$$p(b) \cdot p(a|b) = p(b \wedge a) = p(a) \cdot p(b|a) ,$$

directly leading to equation (4.2.1). Furthermore, every two branches from a node towards the central nodes of the graph have to sum up to one, i.e. $p(a) + p(\neg a) = 1$, or $p(a|b) + p(\neg a|b) = 1$, due to the law of total probability. Therefore,

$$p(b) = p(b \wedge a) + p(b \wedge \neg a) = \sum_{A \in \{a, \neg a\}} p(A) \cdot p(b|A)$$

which can be extended to produce the equations (4.2.2) and (4.2.3). Coming back to the example, the cat's owner can now utilize equation (4.2.2) to calculate the conditional probability $p(a|b)$, assuming that knowledge about the probabilities $p(a)$, $p(b)$, and $p(b|a)$ is available.

Bayesian Parameter Estimation

The crucial part in understanding how Bayes' theorem can be applied to infer unknown parameters, is to properly identify each term. The term $p(A|B)$ can be identified as *posterior distribution*, which describes with what probability a hypothesis A is the true parameter, given the measured evidence B . The term $p(A)$ is the *prior knowledge*, or *prior distribution* of said parameters. The *likelihood function* $p(B|A)$, gives the probability to observe the outcome B given the probability distribution A . Finally, the last term $p(B)$ is called *marginal probability* and is required to normalize the result, as can be seen in equations (4.2.2) and (4.2.3) respectively.

For spectroscopic estimation, as discussed in sections 3.2 and 3.3, the goal is to find the most probable detuning Δ' between the light field and the transition frequency. For the sake of simplicity, we will limit the range within which spectroscopy is performed to a predefined frequency range $[\nu - \Delta_{\max}, \nu + \Delta_{\max}]$ around the last estimate ν of said transition frequency, with $\Delta_{\max} > 0$.¹ Each detuning $\Delta \in [-\Delta_{\max}, \Delta_{\max}]$ is therefore parameterizing a hypothesis $A(\Delta)$ for an algorithm analyzing the data from a Ramsey experiment. In order to facilitate a numerical treatment, the available hypotheses are chosen as a discrete sample of the whole range $[-\Delta_{\max}, \Delta_{\max}]$, with $N \in \mathbb{N}$ elements and a constant step size. Before performing the first experiment, there is no prior knowledge available about which Δ is the most probable. Therefore, the initial prior distribution $p_0(\Delta)$ is chosen as a step function

$$p_0(\Delta) = \begin{cases} \frac{1}{N} & , \Delta \in [-\Delta_{\max}, \Delta_{\max}] \\ 0 & , \text{otherwise} \end{cases}, \quad (4.2.4)$$

treating all Δ within the frequency range as equally probable. Every Ramsey experiment results in a single bit of information $B \in \{|0\rangle, |1\rangle\}$. If an excited state $|1\rangle$ is measured, $p(|1\rangle|\Delta)$ is given by equation (2.5.3). If the outcome is the ground state $|0\rangle$, the likelihood function is given by $p(|0\rangle|\Delta) = 1 - p(|1\rangle|\Delta)$. Therefore, the conditional probability $p(B|\Delta)$ is given by

$$p(B|\Delta) = \begin{cases} p_{\text{Ramsey}, T_2}(\Delta) & , B = |1\rangle \\ 1 - p_{\text{Ramsey}, T_2}(\Delta) & , B = |0\rangle \end{cases}. \quad (4.2.5)$$

Finally, the posterior distribution $p(\Delta|B)$ is given by Bayes' theorem with equation (4.2.2).

Having trapped a single ion, and performing one Ramsey experiment per cycle, a single cycle of the algorithm consists of four basic steps. These steps are now discussed in more detail, providing a better understanding about the algorithm as a whole:

Step 1:

Perform a Ramsey experiment and measure the resulting state $B \in \{|0\rangle, |1\rangle\}$. If an excited state is measured ($B = |1\rangle$) the likelihood function (i.e. the likelihood of observing a bright ion in a Ramsey experiment) is given by equation (2.5.3). When written out, this yields

$$p(|1\rangle|\Delta) = \frac{1}{2} + \left\{ \frac{4\Omega^2}{\tilde{\Omega}^2} \cdot \sin^2\left(\frac{1}{2}\tilde{\Omega}\tau_{\pi/2}\right) \cdot \left[\cos\left(\frac{1}{2}\tilde{\Omega}\tau_{\pi/2}\right) \cdot \cos\left(\frac{1}{2}\Delta\tau + \frac{1}{2}\varphi\right) - \frac{\Delta}{\tilde{\Omega}} \cdot \sin\left(\frac{1}{2}\tilde{\Omega}\tau_{\pi/2}\right) \cdot \sin\left(\frac{1}{2}\Delta\tau + \frac{1}{2}\varphi\right) \right]^2 - \frac{1}{2} \right\} \cdot e^{-\frac{\tau}{T_2}}.$$

If a ground state is measured ($B = |0\rangle$), the likelihood function is given by

$$p(|0\rangle|\Delta) = 1 - p(|1\rangle|\Delta).$$

¹Furthermore, Δ_{\max} is chosen such that the assumptions of the sections 2.4 and 2.5 are met.

Step 2:

Calculate the posterior distribution $p(\Delta|B)$ for the observed outcome B with Bayes' theorem:

$$p(\Delta|B) = \frac{p(\Delta) \cdot p(B|\Delta)}{p(B)}.$$

Figure 4.2.2 depicts how the knowledge about the most probable detuning Δ' increases in this step. In the first cycle of the depicted example (see figure 4.2.2a) an excited state is measured. The step function chosen as initial prior distribution $p_0(\Delta)$ and the likelihood function $p(|1\rangle|\Delta)$ as specified above yield the shown posterior distribution $p(\Delta|1)$.

Step 3:

The updated posterior distribution $p(\Delta|B)$ encompasses our knowledge about the most probable detuning Δ' , given the observed outcome B . In the upcoming cycle of the algorithm, we want to improve upon this knowledge. Therefore, we use the posterior distribution of the current cycle as the prior distribution $p(\Delta)$ of the next cycle, via setting $p(\Delta) \leftarrow p(\Delta|B)$.

Step 4:

Restart with **Step 1** and repeat until the posterior distribution shows the most probable detuning Δ' with a probability density above a desired threshold. Figure 4.2.2 shows a step-by-step example of four update cycles. For the sake of simplicity, it is assumed that all Ramsey experiments resulted in excited state measurements ($B = |1\rangle$).

For $i \in \mathbb{N}$ cycles of the algorithm, the i -th posterior distribution is given by equation (4.2.1) as

$$p_i(\Delta|B_0, \dots, B_i) = \frac{p_{i-1}(\Delta) \cdot p(B_i|\Delta)}{p(B_i)} \quad (4.2.6)$$

where $p_{i-1}(\Delta)$ is equal to the initial prior distribution $p_0(\Delta)$ for $i = 1$, or to the posterior distribution $p_{i-1}(\Delta|E_0, \dots, E_{i-1})$ of the previous cycle otherwise. Therefore, after performing i cycles and detecting $n_{|0\rangle} \in \{n_{|0\rangle} \leq i \mid n_{|0\rangle} \in \mathbb{N}_0\}$ ground states $|0\rangle$, the i -th posterior distribution can iteratively be calculated using equation (4.2.6):

$$p_i(\Delta|B_0, \dots, B_i) = p_0(\Delta) \cdot \left(\frac{p(|0\rangle|\Delta)}{p(|0\rangle)} \right)^{n_{|0\rangle}} \cdot \left(\frac{p(|1\rangle|\Delta)}{p(|1\rangle)} \right)^{i-n_{|0\rangle}}. \quad (4.2.7)$$

Finally, the most probable detuning Δ' given the results of the experiments can be estimated by the final posterior distribution.

In the case of having $n_{\text{ions}} \in \mathbb{N}$ trapped ions available, a single Ramsey sequence performed with the so called global laser beam that is used to illuminate the ions simultaneously yields n_{ions} bits of information. As these measurements are independent of each other, each bit can be interpreted as a separate experiment, as well as a separate cycle in the algorithm described above.

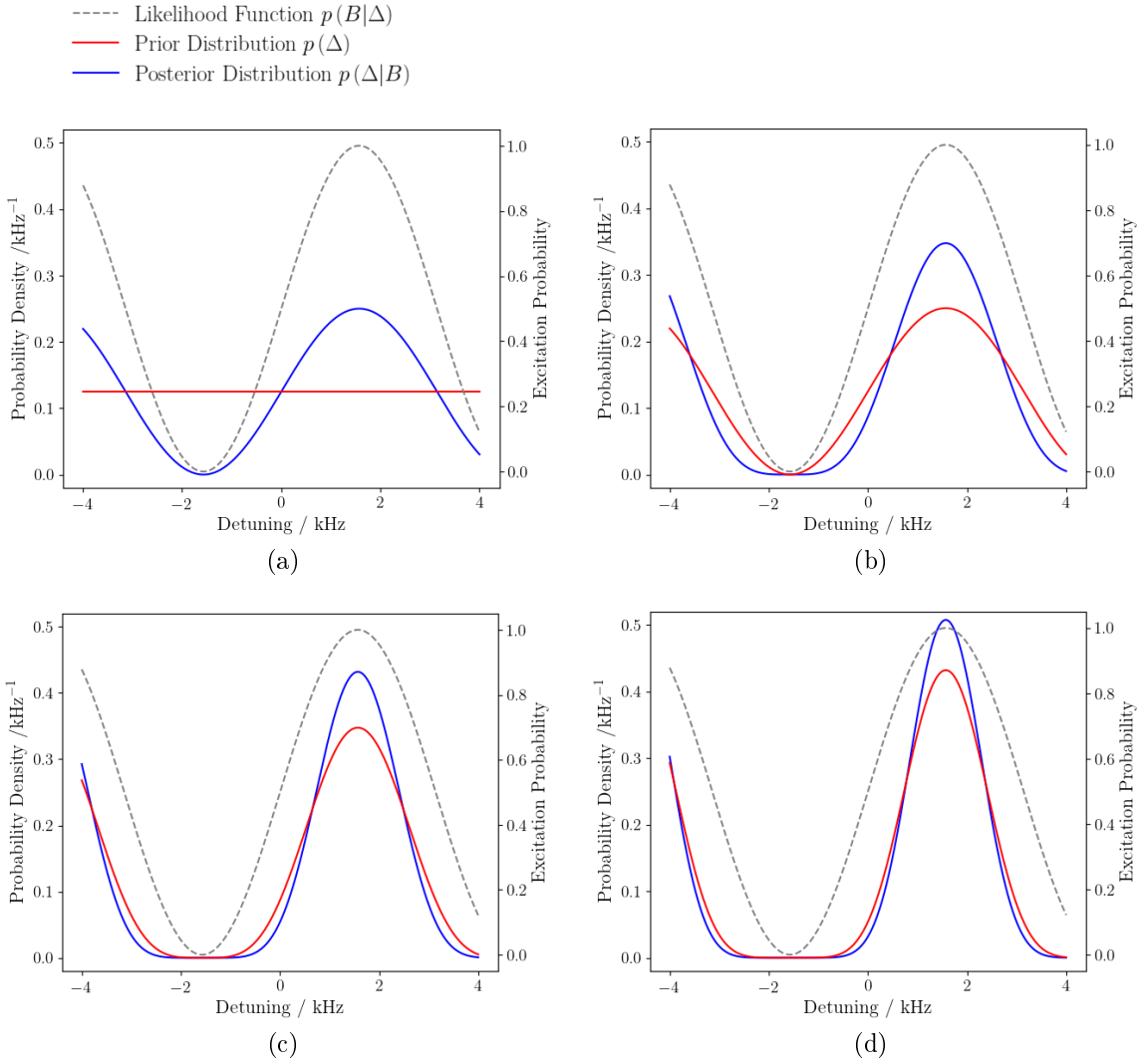


Figure 4.2.2: Simulation of four cycles of the Bayesian Ramsey parameter estimation algorithm discussed in section 4.2. (a) After performing a Ramsey experiment and measuring an excited state ($B = |1\rangle$), the initial prior distribution (red) and likelihood function (grey, dashed) are multiplied and normalized to yield the posterior distribution (blue). (b)-(d) Additional experiments yielding $B = |1\rangle$ increase the knowledge of the most probable detuning Δ' , and narrow it down to $\Delta' = 1.6(8)$ kHz.

In order to show that this algorithm is able to estimate the detuning between the light field and a transition frequency, four ions are loaded in the trap. With the help of Rabi spectroscopy, the global laser beam is deliberately detuned from the $(-1/2, -1/2)$ transition frequency by $\Delta = 2$ kHz. The algorithm is now meant to infer this detuning. Therefore, ten Ramsey experiments are conducted with a π -time of $\tau_\pi = 19.6 \mu\text{s}$, a waiting time of $\tau = 70.2 \mu\text{s}$, a coherence time of $T_2 = 40$ ms, and a phase of $\varphi = 90^\circ$ between the $\pi/2$ -pulses, using said global laser beam. The resulting posterior distribution after the corresponding 40 cycles of the algorithm described above can be found in figure 4.2.3.

The shown posterior distribution features several maxima with one of them located at a detuning of about 2 kHz. The appearance of the other maxima results from the

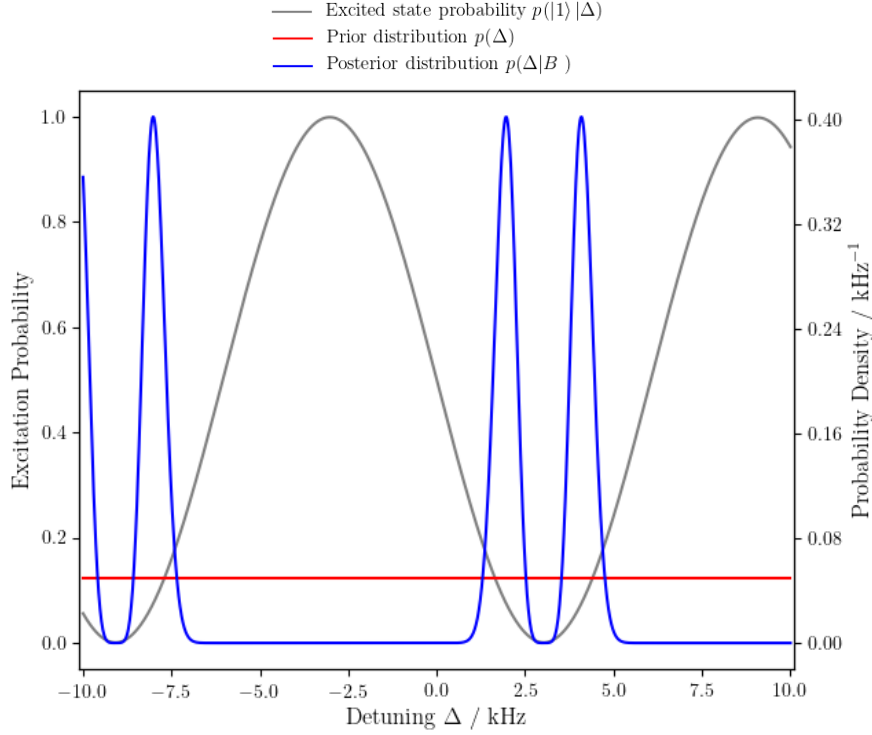


Figure 4.2.3: Initial prior distribution, likelihood function, and final posterior distribution after 40 Ramsey experiments, as described in section 4.2. All 40 experiments have been conducted with the same parameters, leading to multiple candidates for a most probable detuning between light field and $(-1/2, -1/2)$ transition frequency.

ambiguity of Ramsey fringes as elaborated on in section 3.3. Therefore, as the inferred most probable detuning is ambiguous, the algorithm has to be refined to produce unique results that can be used for automated frequency stabilization.

Adaptive Bayesian Ramsey Spectroscopy Algorithm

In order to eliminate all but one maximum in the final posterior distribution, the experimental parameters have to be adapted to the corresponding prior distribution after a few cycles of the algorithm described above. Therefore, an adaptive algorithm is required that chooses optimal parameters for upcoming experiments after evaluating data. In every cycle of this adaptive algorithm, the most informative experiment with respect to the available prior knowledge will be selected. With n_{ions} trapped ions available, it is convenient to adapt the parameters after every $n_{\text{exp}} \geq n_{\text{ions}}$ Ramsey experiments, leading to the following steps:

1. Calculate the optimal parameters for upcoming experiments.
2. Perform n_{exp} Ramsey experiments and measure the resulting states $B_1, \dots, B_{n_{\text{exp}}}$.
3. Calculate $p(\Delta|B_1, \dots, B_{n_{\text{exp}}})$ from equation (4.2.7).
4. Set $p(\Delta) \leftarrow p(\Delta|B_1, \dots, B_{n_{\text{exp}}})$.

5. Restart with 1.

The two parameters of a Ramsey experiment that can be tuned without requiring a re-calibration of the system, are the waiting time τ between the pulses, and the phase offset φ of the second pulse. As described in section 3.3 and visualized in figure 3.3.1b, a reduction of τ stretches the Ramsey fringes and reduces their number, while the phase of the fringes is dictated by φ . The likelihood function given by equation (4.2.5) behaves correspondingly. Therefore, the parameters τ and φ have to be chosen such, that a single measurement outcome decreases the variance of the posterior distribution, without introducing multiple maxima. Figure 4.2.4 illustrates the update of a prior distribution with a single maximum by a single excited state measurement for several choices of τ and φ .

With fewer fringes, the chance to generate a posterior distribution with multiple peaks is lower. Therefore, we choose the strategy to initialize the algorithm with the lowest possible waiting time τ_{\min} and increase τ with every cycle. The optimal values for the i -th cycle's waiting time τ_i and phase offset φ_i (see figure 4.2.4a) can be calculated from equation (4.2.5): For the sake of simplicity, we assume a Gaussian prior distribution

$$p(\Delta) = \frac{1}{\sqrt{2\pi\sigma^2}} \cdot \exp\left(-\frac{\Delta^2}{2\sigma^2}\right) \quad (4.2.8)$$

that is centered around $\Delta = 0$, where σ^2 is the prior distribution's variance. Assuming $\Delta \ll \Omega$ as well as $\tau_{\pi/2} \ll \tau_i \ll T_2$, the likelihood function $p(|1\rangle|\Delta)$ for a measured excited state $|1\rangle$ can be approximated by [26]

$$p(|1\rangle|\Delta) \approx \frac{1}{2} (1 + \cos(\Delta\tau_i + \varphi_i)) . \quad (4.2.9)$$

The resulting posterior distribution $p(\Delta|1)$ is calculated from equation (4.2.1), yielding

$$p(\Delta|1) \propto \frac{1}{2\sqrt{2\pi\sigma^2}} \cdot (1 + \cos(\Delta\tau_i + \varphi_i)) \cdot \exp\left(-\frac{\Delta^2}{2\sigma^2}\right) \quad (4.2.10)$$

when neglecting the normalization. Therefore, the variance $\tilde{\sigma}^2$ of the posterior distribution is given by

$$\begin{aligned} \tilde{\sigma}^2 &= \int_{-\infty}^{\infty} \Delta^2 p(\Delta|1) d\Delta - \left(\int_{-\infty}^{\infty} \Delta p(\Delta|1) d\Delta \right)^2 \\ &\propto \frac{\sigma^2}{2} \left(1 + (1 - \sigma^2\tau_i^2) \cdot \cos(\varphi_i) \cdot e^{-\frac{\sigma^2\tau_i^2}{2}} - \frac{\sigma^2\tau_i^2}{2} \cdot \sin^2(\varphi_i) \cdot e^{-\sigma^2\tau_i^2} \right) . \end{aligned}$$

As shown in figure 4.2.4b, if φ_i is chosen such that the minimum of a Ramsey fringe is located at the detuning of the prior distribution's maximum, a measured excited state can lead to two maxima in the resulting posterior distribution. In order to avoid this case in the given example, $\varphi_i = \pi/2$ is chosen, placing the turning point of the Ramsey fringe at the location of the prior distribution's maximum and yielding

$$\tilde{\sigma}^2 \propto \frac{\sigma^2}{2} \left(1 - \frac{\sigma^2\tau_i^2}{2} \cdot e^{-\sigma^2\tau_i^2} \right) . \quad (4.2.11)$$

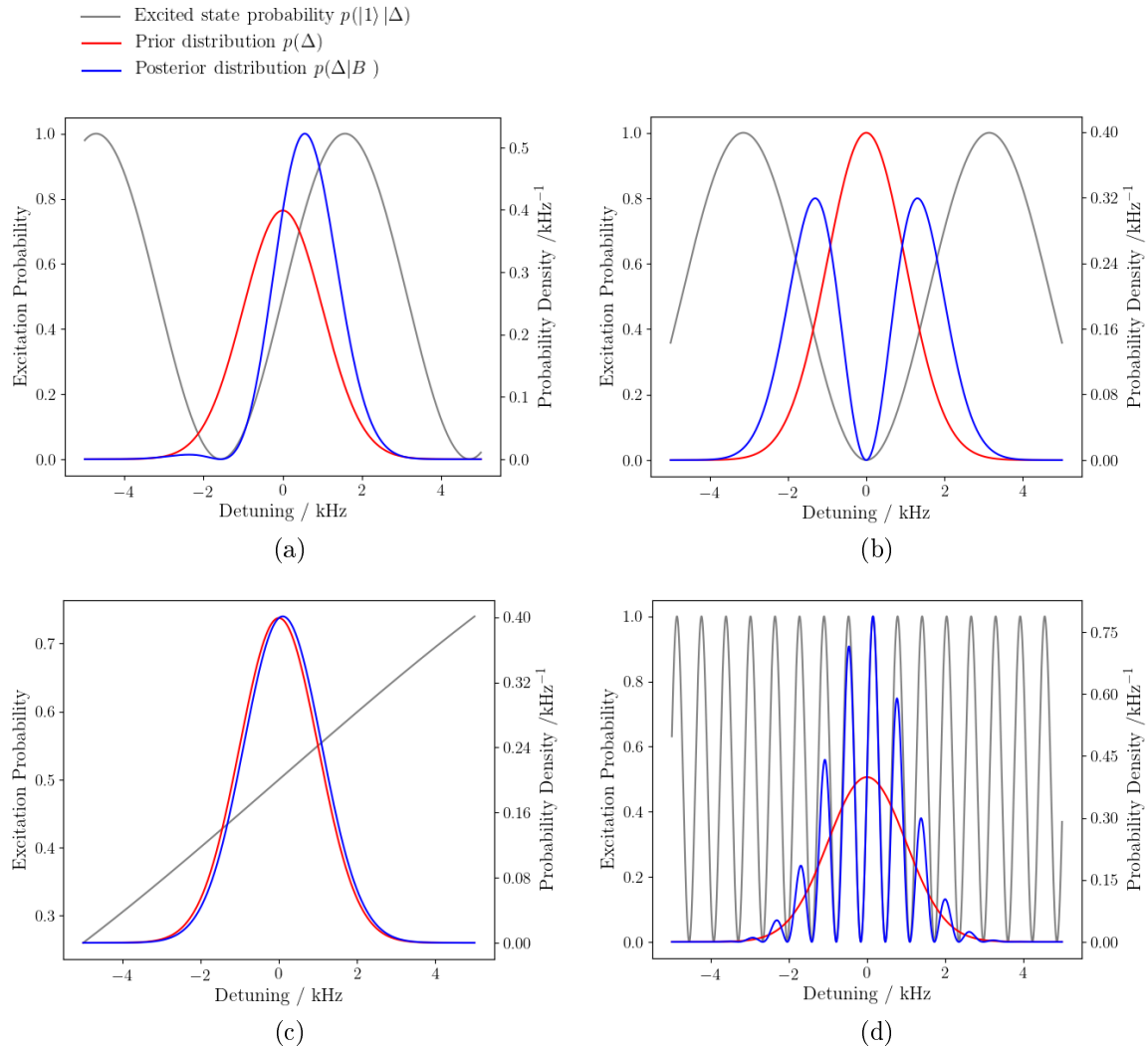


Figure 4.2.4: Numerical simulation of a Bayesian update using a Gaussian prior distribution with a sinusoidal likelihood function, leading to different posterior distributions depending on the period and phase of the likelihood function. (a) If the phase and period are chosen such that the turning point of the likelihood function is at the location of the prior distribution's maximum and the majority (in this example chosen to be two standard deviations) of the prior distribution fits into one oscillation of the likelihood function, the resulting posterior distribution shows a Gaussian-like shape with a reduced FWHM. (b) If the period is chosen as in case (a) and the phase of the likelihood function such that a minimum is located at the position of the prior distribution's maximum, the resulting posterior distribution shows two Gaussian-like peaks. (c) If the likelihood function has a much larger period with respect to the prior distribution's width, the posterior distribution shows a Gaussian-like shape. However, the FWHM of the posterior distribution is not significantly smaller than the FWHM of the prior distribution. (d) A likelihood function that has a much smaller period with respect to the width of the prior distribution leads to multiple peaks in the posterior distribution.

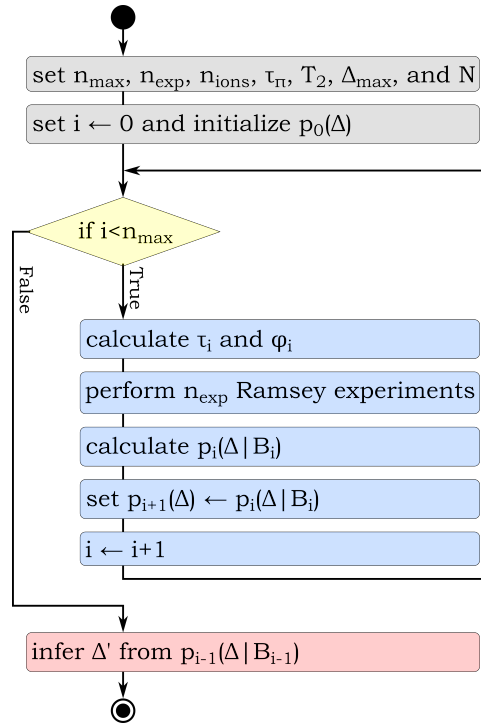


Figure 4.2.5: State diagram of an adaptive algorithm inferring a detuning between transition frequency and light field using Ramsey experiments, parameter optimization, and Bayesian data analysis. The initial parameters (grey) of the algorithm are the number of cycles n_{\max} after which the algorithm terminates, the number of Ramsey experiments conducted per cycle n_{exp} , the number of ions n_{ions} , the π -time τ_{π} , the phase coherence time T_2 , the maximum detuning Δ_{\max} , and the number of steps N within the interval $[-\Delta_{\max}, \Delta_{\max}]$. The initial prior distribution $p_0(\Delta)$ is set according to equation (4.2.4). During each cycle i (blue), Ramsey experiments are performed with the most informative waiting time τ_i and phase φ_i , as described in section 4.2. The i -th posterior distribution $p_i(\Delta|B_i)$ is then calculated from Bayes' theorem. After the final cycle (red), the most probable detuning Δ' between the laser system and the transition frequency is inferred from the final posterior distribution.

The i -th cycle's optimal waiting time $\tau'_i = 1/\sigma$ minimizes the posterior distribution's variance given by equation (4.2.11). If the waiting time is chosen too small ($\tau_i \ll \tau'_i$), less information can be gained from the experiment, resulting in the algorithm converging slower (see figure 4.2.4c). If the waiting time is chosen too large ($\tau_i \gg \tau'_i$), multiple maxima are generated (see figure 4.2.4d).

Lastly, if such an adaptive algorithm is to be used in the context of frequency stabilization as discussed in section 3.1, a condition for termination has to be defined. In a straight forward approach, the maximal number of cycles n_{\max} is defined, after which the algorithm aborts and estimates the most probable detuning from the final posterior distribution. A state diagram describing said adaptive algorithm can be found in figure 4.2.5.

Using the adaptive algorithm shown in figure 4.2.5, the experiment discussed above (see figure 4.2.3) can be continued. Choosing the initial parameters listed in table 4.1, the goal is to infer a known detuning of 2 kHz between the laser and $(-1/2, -1/2)$ tran-

sition frequency. The experimental results, as well as the automatically chosen experimental parameters of each cycle are listed in table 4.2. The corresponding prior and posterior distributions are illustrated in figure 4.2.6.

After the first cycle (see figure 4.2.6a), multiple maxima appear in the posterior distribution. The adaptive choice of the waiting time and phase eliminates all but one maximum in the second cycle (see figure 4.2.6b). In the third and fourth cycle the waiting time is further increased leading to a more precise estimation of the fixed detuning of 2 kHz between light field and transition frequency. A more thorough discussion on the resolution and stability that is achievable with the implemented algorithm follows in the next chapter.

Table 4.1: Parameters used by the adaptive Bayesian Ramsey spectroscopy algorithm to deduce a 2 kHz detuning between light field and $(-1/2, -1/2)$ transition frequency. The parameters, algorithm, and experiment are discussed in section 4.2.

n_{\max}	n_{exp}	n_{ions}	τ_{π}	T_2	Δ_{\max}	N
4	40	4	19.6 μs	40 μs	10 kHz	1000

Table 4.2: Experimental parameters and results of four update cycles of the adaptive Bayesian Ramsey algorithm. The waiting time τ_i and the phase offset φ_i of the i -th cycle are calculated from the prior distribution displayed in the corresponding figure. The number of measured ground states $n_{|0\rangle}$ and excited states $n_{|1\rangle}$ are used to calculate the posterior distribution shown in the respective figure utilizing equation (4.2.7).

τ_i in μs	φ_i	$n_{ 0\rangle}$	$n_{ 1\rangle}$	figure
70.2	90.0°	37	3	4.2.6a
70.2	211.7°	24	16	4.2.6b
187.2	144.8°	17	23	4.2.6c
707.8	157.8°	10	30	4.2.6d

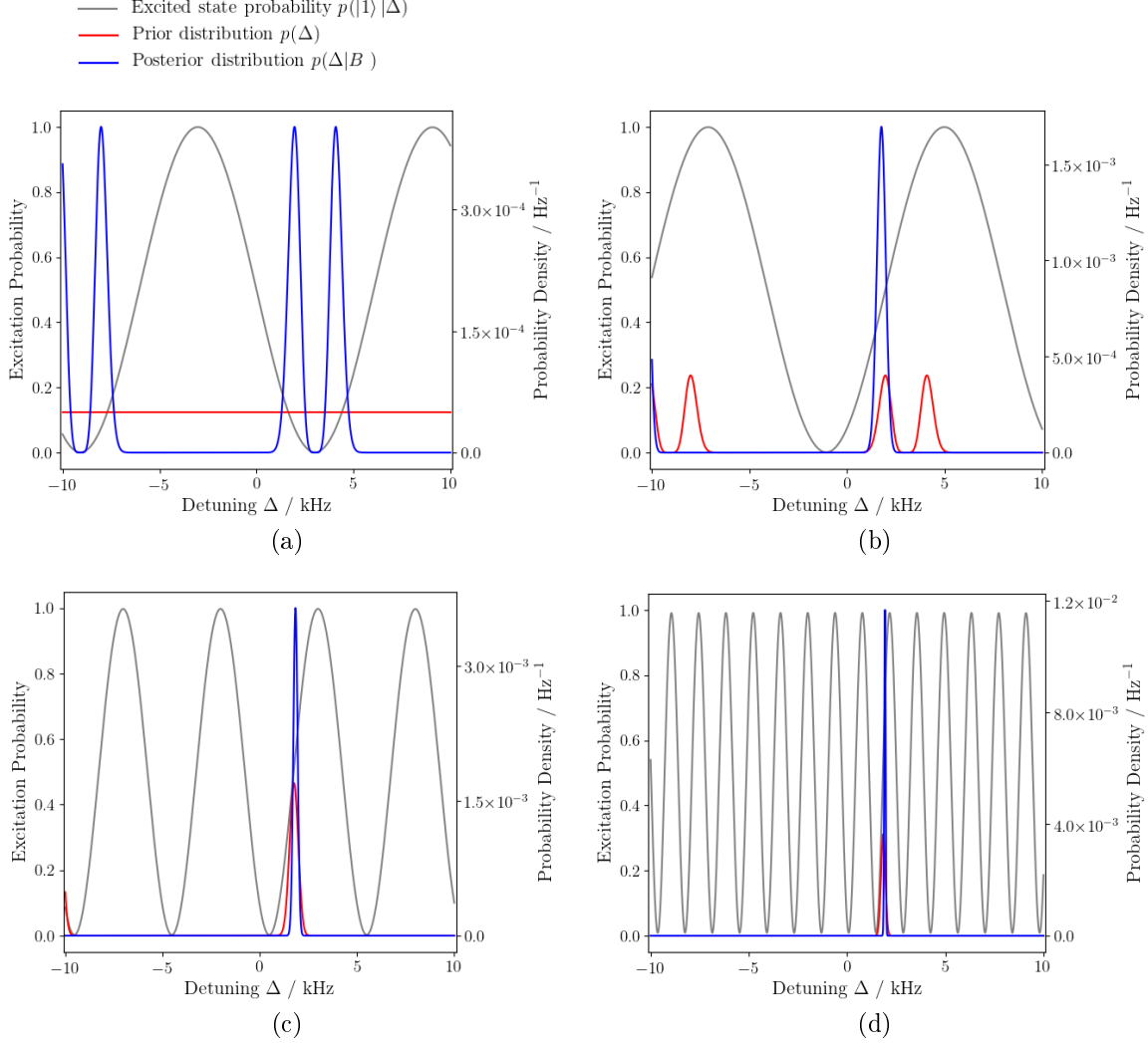


Figure 4.2.6: Four experimental update cycles of the adaptive Bayesian Ramsey spectroscopy algorithm, deducing a detuning of $\Delta = 2$ kHz between the laser system and the $(-1/2, -1/2)$ transition frequency of four trapped ions. Each sub-figure shows the prior distribution $p_i(\Delta)$, excited state probability $p_i(|1\rangle|\Delta)$, and posterior distribution $p_i(\Delta|B_i)$ of the i -th cycle, with B_i being the measurement results of said cycle, against the detuning Δ . (a) After the first cycle, the posterior distribution shows multiple maxima, as discussed in section 4.2. (b) The adaptive choice of the second cycle's experimental parameters yields a single maximum. (c)-(d) The resolution is increased by increasing the Ramsey time while tuning the phase accordingly, leading to a more precise measurement of the detuning.

4.3 Bayesianism vs. Least Squares Minimization

The least squares method is one of the most common methods to analyze statistical data. One of the main assumptions of the least squares method is that the statistical uncertainty of the data follows a Gaussian distribution as given with equation (4.1.1). In the given experimental setup, each individual state measurement either yields $|0\rangle$ or $|1\rangle$. By repeating the experiment $n_{\text{exp}} \in \mathbb{N}$ times, a mean excitation p_m is calculated from $p_m = n_{|1\rangle}/n_{\text{exp}}$, where $n_{|1\rangle} \in \{n_{|1\rangle} \leq n_{\text{exp}} \mid n_{|1\rangle} \in \mathbb{N}_0\}$ is the number of measured excited states $|1\rangle$. Therefore, the distribution that governs p_m is given by the binomial distribution

$$P_{\text{Binomial}}(k; n, p) = \binom{n}{k} p^k (1-p)^{n-k}$$

where $n \in \mathbb{N}$ is the number of samples, $k \in \mathbb{N}_0$ the random variable, $p \in [0, 1]$ the probability of success, and

$$\binom{n}{k} = \frac{n!}{k!(n-k)!}$$

the binomial coefficient. In the given context, the probability to measure $n_{|1\rangle}$ excited states $|1\rangle$, when performing n_{exp} measurements of a qubit that is with a probability of p_{m_0} in the excited state, is given by

$$P_{\text{Binomial}}(n_{|1\rangle}; n_{\text{exp}}, p_{m_0}) .$$

In the case of large samples $n_{\text{exp}} \rightarrow \infty$, the binomial distribution can be approximated by a Gaussian distribution [56], as

$$P_{\text{Binomial}}(n_{|1\rangle}; n_{\text{exp}}, p_{m_0}) \xrightarrow{n_{\text{exp}} \rightarrow \infty} P_{\text{Gauss}}\left(n_{|1\rangle}; n_{\text{exp}} \cdot p_{m_0}, \sqrt{n_{\text{exp}} \cdot p_{m_0} \cdot (1 - p_{m_0})}\right),$$

leading to the least squares method's assumption to be fulfilled only in this case.

Figure 4.3.1 shows simulated data with a probability of $p_{m_0} = 0.04 \cdot t + 0.1$, where $t \in [0, 10]$. Every displayed mean excitation data point is a result of $n_{\text{exp}} = 5$ measurements drawn from a binomial distribution. The data is analyzed by both an unweighted least squares algorithm, yielding an estimated excitation probability of $0.07(2) \cdot t - 0.1(1)$, and an algorithm based on Bayesian inference taking the binomial distribution into account, yielding an estimate of $0.05(1) \cdot t + 0.06(5)$. The Bayesian algorithm's results are within one standard deviation of p_{m_0} and show uncertainties that are by a factor of two smaller than the ones of the least squares algorithm's results.

Another disadvantage of a straight forward least squares algorithm using minimization techniques like the Levenberg-Marquardt algorithm [57, 58] is its dependence on the initial parameters. If the initial parameters are not close enough to the true parameters, the algorithm might converge to a local minimum of equation (4.1.2). In this case, the algorithm does not yield an accurate estimate for the true parameters. For a least squares algorithm this problem can be solved by a using a tailored minimization algorithm or a more precise determination of the initial parameters. The presented Bayesian algorithm on the other hand explores the whole parameter space for which the prior distribution is not zero, making it less affected by an imprecise choice of initial parameters.

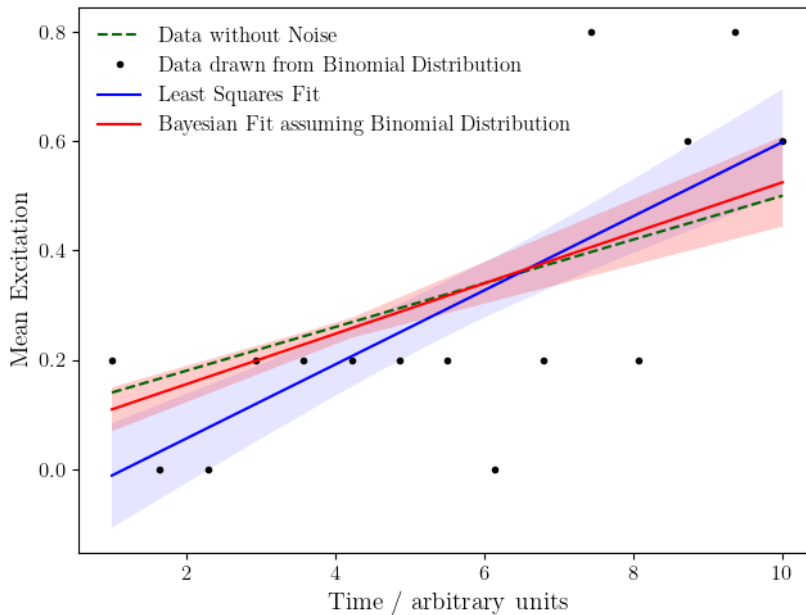


Figure 4.3.1: Comparison between Bayesian and least squares linear function fitting routines, as described in section 4.3. The data points (black) are randomly distributed around p_{m_0} (dashed) by the binomial distribution as a result of $n_{\text{exp}} = 5$ measurements per point. A least squares fit (blue) assuming Gaussian noise as well as a Bayesian fit (red) assuming binomial noise are then used to infer p_{m_0} from the data points. The shaded area indicates the 1σ credible interval of the respective fit.

A strong dependence on precise initial parameters can make it challenging to analyze complex data as generated by Ramsey experiments. In order to show how the presented Bayesian and least squares algorithms cope with imprecise initial parameters, Ramsey experiments are performed on the $(-1/2, -1/2)$ transition of two trapped ions with a waiting time $\tau = 70.2 \mu\text{s}$, a phase offset $\varphi = 0$ between the $\pi/2$ -pulses, and a π -time of $\tau_\pi = 30.9 \mu\text{s}$. The resulting Ramsey spectrum is shown in figure 4.3.2 and spans over a frequency range of about $\sim 400 \text{ kHz}$ with every mean excitation data point being the result of $n_{\text{exp}} = 100$ Ramsey experiments. The data is then fitted by a least squares algorithm using a Levenberg-Marquardt minimization algorithm, as well as by an algorithm using Bayesian inference as described in section 4.2. For the least squares algorithm, an initial guess for the center of the spectrum has to be chosen. In figure 4.3.2, this initial guess is 44.2 kHz detuned from the $(-1/2, -1/2)$ transition frequency. Similarly, the Bayesian algorithm's prior distribution is initialized with a Gaussian distribution that is centered at the same initial guess, has a standard deviation of 100 kHz , and is cut-off at the maximal detuning that is covered by the data. One hundred fits are then performed with different, normally distributed, initial guesses. The Gaussian distribution of the initial guesses is centered at the true value. In figure 4.3.3 the differences between true value and the corresponding fit results are plotted against the difference between the true value and the corresponding initial guess. As can be seen, the fit results for of the Bayesian algorithm do not show any remarkable dependence on the initial guesses. For any used initial parameter, the difference between the fit result and the true value is below 0.2 kHz , being one

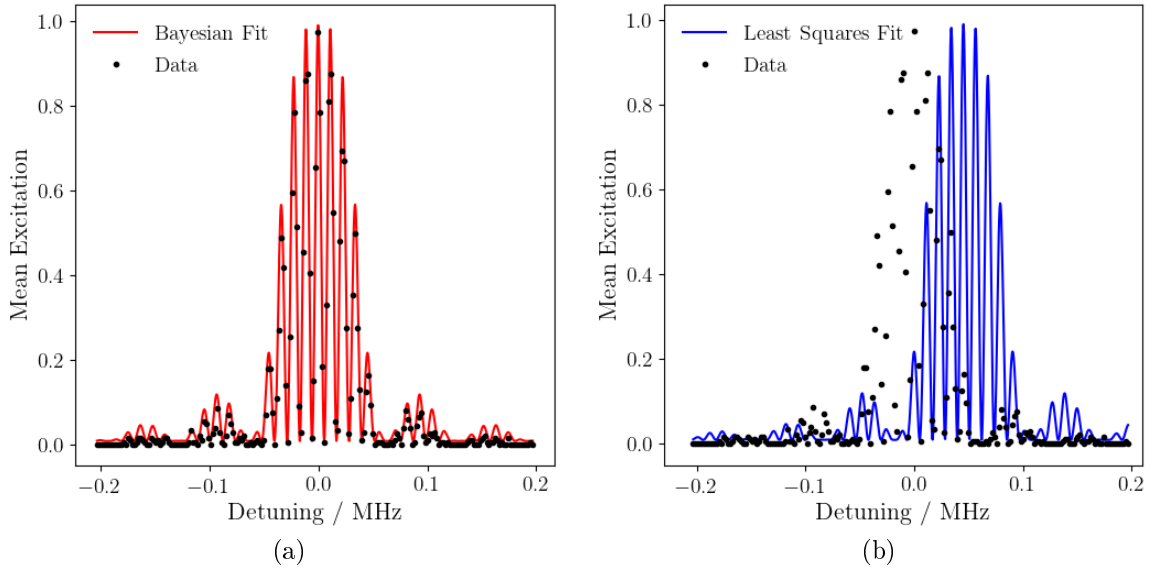


Figure 4.3.2: Ramsey spectrum with corresponding (a) Bayesian and (b) least squares fits. The mean excitation data points (black) resulting from the Ramsey experiments described in section 4.3 are plotted against the corresponding detuning between the light field and the $(-1/2, -1/2)$ transition frequency. The spectrum is fitted using an algorithm based on Bayesian inference (red) as well as a least squares algorithm utilizing a Levenberg-Marquardt minimization algorithm (blue). The initial guess for the center of the spectrum is chosen as 44.2 kHz for both algorithms.

order of magnitude lower than the difference between two neighboring data points of the spectrum. The least squares algorithm's results show a linear dependence on the initial guesses. The step-like substructure is an indication of the algorithm converging to local minima, resulting in fringe hopping as indicated in figure 4.3.2. In order to correctly estimate the $(-1/2, -1/2)$ transition frequency in the given example, the initial parameters of the used least squares algorithm have to be less than 6 kHz detuned from the true value, which corresponds to half the period of the Ramsey fringes.

Concluding this chapter, a least squares algorithm implies normally distributed data points, and depending on the chosen minimization algorithm is vulnerable to imprecise initial parameters, leading e.g. to fringe hopping as described above. The major advantages of least squares algorithms are that they are typically computationally faster than their Bayesian equivalent. Furthermore, least squares algorithms are already included in most data analysis tools, making them well suited for quick data analysis within the framework of choice. When using least squares algorithms however, one has to be aware of their limits and assumptions.

Bayesian algorithms on the other hand are able to handle non-Gaussian distributed data and can directly incorporate complex models like the Ramsey excitation probability as given with equation (2.5.3). Furthermore, Bayesian algorithms are typically less prone to converging to local minima, as long as the specified model and prior distribution are describing the data sufficiently well. Using a Bayesian algorithm is a straight forward solution for the problems described above. Tailoring a least squares algorithm to solve these problems is not only involved, but also restricts the algorithm to this

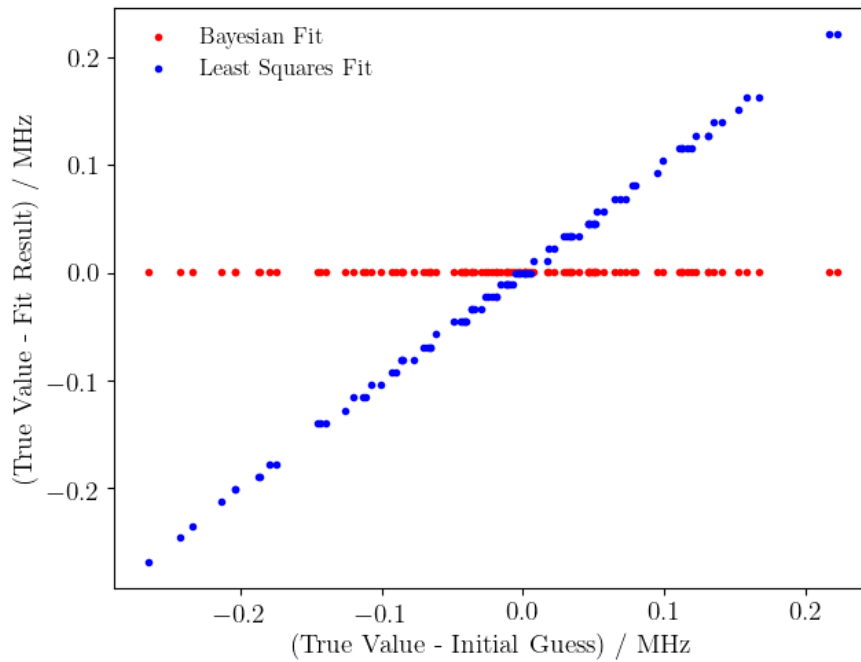


Figure 4.3.3: Dependence of Bayesian and least squares fit results on initial parameters. As described in section 4.3, the difference between true and estimated values is plotted against the difference between true value and corresponding initial guess used by a least squares algorithm (blue) and a Bayesian algorithm (red). The corresponding standard deviations from the respective fitting algorithms are too small to be displayed as errorbars.

purpose only. Implementing a Bayesian framework on the other hand, also opens the door for other Bayesian parameter estimation routines, which can be used to automate other aspects of the given quantum computer experiment, like measurements of the Rabi frequency or optimization tasks for quantum gate operations.

Chapter 5

Experimental Results

The experiments that are conducted within this thesis revolve around automating frequency stabilizing tasks as introduced in section 3.1. Thus, a computer program is written that periodically performs spectroscopic measurements on the trapped ions, analyzes the results and calculates the drifts and offsets between selected transition frequencies of the ions and the applied light field in order to stabilize the latter to said transitions.

Two spectroscopic techniques have been implemented for this computer program. In the initialization mode, Rabi spectroscopy is performed and the resulting data is analyzed using a least squares fitting algorithm, as discussed in the sections 3.2 and 4.1. The second mode is optimized for accuracy and speed, using the adaptive Bayesian Ramsey spectroscopy algorithm discussed in section 4.2. The initialization requirements and measurement uncertainties are discussed within this chapter.

Over the course of more than six months, the drifts and offsets between the Zeeman sub-level transitions introduced in section 2.2 and the light field generated by a laser system operating at a wavelength of 729 nm have been measured and compensated. Concluding this chapter, the short and long term behavior of these drifts and offsets is analyzed.

5.1 Rabi Spectroscopy

In its initialization mode, the computer program performs Rabi spectroscopy on two of the Zeeman sub-level transitions shown in figure 2.2.2. As discussed in chapter 3, the default transitions to perform spectroscopy on are $(-1/2, -1/2)$ and $(-1/2, -5/2)$. The spectroscopic measurements result in mean excitation data points as shown in figure 3.2.2, that are then analyzed using a least squares algorithm utilizing the Levenberg-Marquardt minimization algorithm and a Lorentzian model function. The fit results are then used to solve the system of equations (3.1.4) for actual values of the center frequency and magnetic field strength, which enables the compensation of drifts and offsets as discussed in section 3.1.

The main principles of Rabi spectroscopy are already discussed in section 3.2. In practice, the main use case for the Rabi spectroscopy mode is to infer the transition frequencies to an accuracy that is sufficient to initialize the adaptive Bayesian Ramsey spectroscopy algorithm discussed in section 4.2. Therefore, the initialization has to

cope with limited prior knowledge on the transition frequencies, preferably reducing the uncertainty of all transition frequencies to a few Kilohertz.

Initialization

As described in section 3.2, approximate knowledge of the transition frequencies is required when performing Rabi spectroscopy on a single transition, in order to ensure that said transition frequencies are well within the corresponding sampled frequency ranges. Therefore, when initializing the Rabi spectroscopy mode, it is advisable to measure a broad spectrum as shown in figure 3.2.1 and to assign the local maxima to the corresponding transitions.

If the latest measurement of the transition frequencies is a few days old, the latest estimated value of the drift between the transition frequencies and the laser system can be used to estimate the required frequency range that has to be sampled. Giving a short example, if the latest spectroscopic data is two days old and the latest estimate of the drift is 0.4 Hz/s, the transition frequencies are detuned by approximately 69 kHz, assuming the drift is constant. Therefore, sampling a frequency range of approximately 200 kHz with a step size of 1 kHz should be sufficient to relocate the corresponding transition frequency.

With approximate knowledge of the transition frequencies available, Rabi spectroscopy can be performed on single transitions as described in section 3.2, resulting in narrow spectra as shown in figure 3.2.2.

Uncertainty Estimation

In figure 3.2.1 a mean excitation spectrum over a 48 MHz frequency range in steps of 2 kHz, taken from two trapped $^{40}\text{Ca}^+$ ions, can be found. The data shown in figure 3.2.1 has been measured, while the frequency of the corresponding laser system has been stabilized using Rabi spectroscopy as described in chapter 3. Every ten minutes, Rabi spectroscopy is performed on the two trapped ions. Drifts and offsets are compensated for correspondingly.

By analyzing the data shown in figure 3.2.1, the uncertainty of this continuous calibration can be estimated. The frequencies of the maxima that are identified as the $(-1/2, -1/2)$ and $(-1/2, -5/2)$ transitions respectively, are thereby used to calculate the other transition frequencies. The differences between the measured and calculated frequencies are shown in figure 5.1.1.

As the step size of the data in figure 3.2.1 is 2 kHz and the difference of the measured and calculated carrier transition frequencies is on that order as well, the uncertainty of the Rabi spectroscopy mode's calibration can be assumed to be in the same order of magnitude or less. This shows that it is possible to reduce the uncertainty of the carrier transition frequencies to a few Kilohertz, which is sufficient to prepare the system for the adaptive Bayesian Ramsey spectroscopy algorithm.

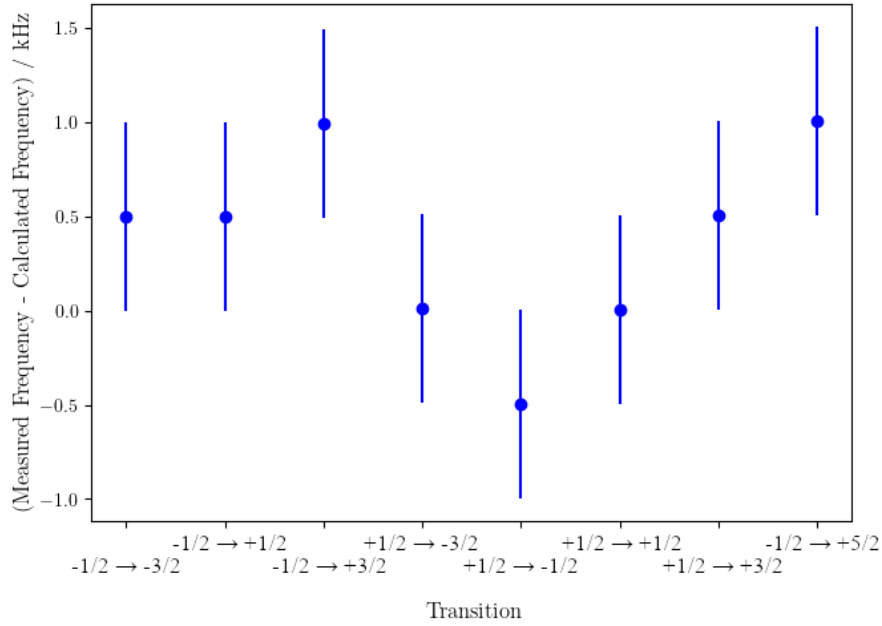


Figure 5.1.1: Differences between measured and calculated carrier transition frequencies. The data of the spectrum shown in figure 3.2.1 is analyzed, using the frequencies of the maxima identified as $(-1/2, -1/2)$ and $(-1/2, -5/2)$ transition and equation (3.1.4), to calculate the other transition frequencies.

5.2 Adaptive Bayesian Ramsey Spectroscopy

The adaptive Bayesian Ramsey spectroscopy mode uses the algorithm introduced in section 4.2 to continuously calibrate the experiment, while being both faster and more accurate than the Rabi spectroscopy mode. The price to be paid for this, is a more complex initialization procedure, that requires prior knowledge of the transition frequencies to an accuracy on the order of a few Kilohertz, as well as prior knowledge of additional experimental parameters like e.g. the Rabi frequency.

A proof of principle experiment, showing that the adaptive Bayesian Ramsey spectroscopy algorithm can be used to deduce the detuning between transition frequency and light field is discussed in section 4.2, and its results are illustrated in figure 4.2.6. Thereby, the algorithm is shown to correctly deduce a detuning of 2 kHz. The discussion of this section focuses on the algorithm's capability to stabilize the laser frequency over multiple hours.

Initialization

As can be seen in figure 4.2.5 showing the state diagram describing this mode's algorithm, there are a few parameters to consider in the initialization:

- the number of ions
- the desired number of cycles after which the algorithm terminates
- the number of experiments that should be conducted per cycle

- the frequency range within which the respective transition frequency is expected to be
- the number of samples that are drawn from the frequency range which is based on the available prior knowledge of the transition frequency and the desired resolution
- the phase coherence time T_2
- and the $\pi/2$ -time $\tau_{\pi/2}$

The number of ions loaded in the trap is known from fluorescence measurements as shown in figure 2.1.3. The number of experiments per cycle follows from the number of ions as discussed in section 4.2 and indicates how many bits of information are gathered before the data is analyzed and the experimental parameters are adapted in the next cycle. Depending on the number of experiments per cycle, the number of cycles has to be specified, to ensure that the algorithm converges.

The frequency range has to be chosen large enough to include the transition frequency. With increasing the number of samples that are drawn from the frequency range, the computational time required for Bayesian parameter estimation increases. Therefore, the choice of the frequency range and number of samples is a trade-off between available knowledge and computational time. Furthermore, due to limitations in the control hardware, the minimal waiting time between $\pi/2$ -pulses can be up to a few tens of microseconds. This leads to a reduced robustness against fringe hopping for large frequency ranges on the order of tens of Kilohertz.

The phase coherence time T_2 has to be measured by performing Ramsey experiments with increasing waiting times. In contrast to the other parameters, T_2 is constant over days and therefore does not have to be re-calibrated often. Furthermore, as the used waiting times are typically at least one order of magnitude smaller than T_2 , only approximate knowledge on T_2 is required.

The $\pi/2$ -time $\tau_{\pi/2}$ has to be measured by performing Rabi oscillations, followed by sinusoidal least squares fits of the data. This measurement requires knowledge of the transition frequencies. Therefore, an initial stabilization of the light field frequency by the Rabi spectroscopy mode is required.

Uncertainty Estimation

In order to estimate how well the adaptive Bayesian Ramsey spectroscopy algorithm is able to stabilize the frequency of a laser system to a transition frequency, Ramsey experiments are performed while simultaneously stabilizing the light field's frequency with the algorithm. The Ramsey experiments thereby periodically probe the $(-1/2, -1/2)$ and $(-1/2, -5/2)$ transition frequencies for over ~ 5.5 h, using a waiting time of $\tau = 0.5$ ms, and a phase offset $\varphi = 90^\circ$ between the $\pi/2$ -pulses. The idea is that if the light field frequency is perfectly stabilized to the respective transition frequency, a mean excitation of 0.5 is measured when accumulating the data of one hundred successive Ramsey experiments. Furthermore, any deviation from this value of 0.5 can be translated to an imperfect frequency tracking.

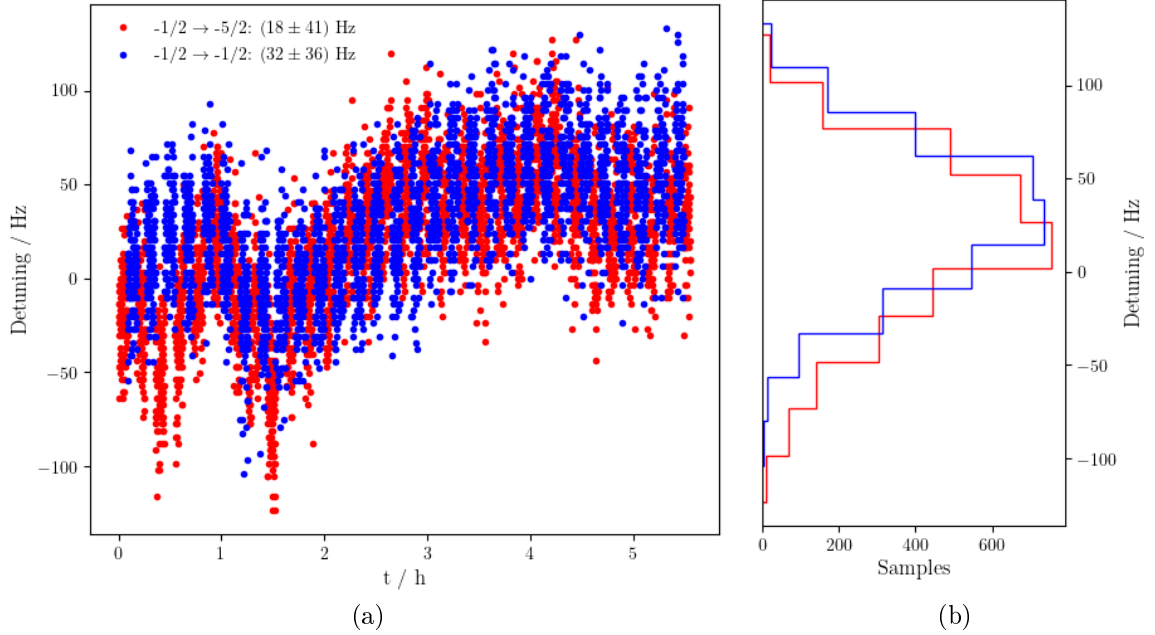


Figure 5.2.1: Difference between the expected and measured $(-1/2, -1/2)$ (blue) and $(-1/2, -5/2)$ (red) transition frequencies. (a) The shown data is a result from calculating mean excitation values after accumulating one hundred successive Ramsey experiments. (b) A histogram of the data shown in (a).

One hundred Ramsey experiments are performed every second, alternating between the transitions $(-1/2, -1/2)$ and $(-1/2, -5/2)$ after every 10^4 experiments. The results of the measured detunings are shown in figure 5.2.1. Every two minutes, these experiments are interrupted by the adaptive Bayesian Ramsey spectroscopy algorithm, that is initialized with the parameters shown in table 5.1. As discussed in section 3.1, the light field frequency is stabilized by estimating the offsets and drift rates of the center frequency ν_{center} and magnetic field strength B , using a linear least squares fit of spectroscopic measurements. A look-back time t_{LB} defines which data is recent enough to perform the linear fits estimating these parameters. The chosen look-back time for the center frequency is $t_{\text{LB},\nu} = 2 \text{ h}$ and for the magnetic field $t_{\text{LB},B} = 1 \text{ h}$. The reasoning for the choice of these look-back times follows in the next section.

Table 5.1: Initial parameters of the adaptive Bayesian Ramsey spectroscopy algorithm. A description of each parameter can be found in section 4.2.

Parameter	$(-1/2, -1/2)$	$(-1/2, -5/2)$
n_{cycles}	10	10
n_{exp}	20	20
n_{ions}	2	2
τ_{π}	49.5 μs	76 μs
T_2	4 ms	4 ms
Δ_{max}	5 kHz	5 kHz

Figure 5.2.1 shows a mean detuning of $\overline{\Delta}_{-1/2} = (32 \pm 36)$ Hz for the $(-1/2, -1/2)$ transition and $\overline{\Delta}_{-5/2} = (18 \pm 41)$ Hz for $(-1/2, -5/2)$. A significant contribution of the uncertainties is a variation of the estimated drift rates of the center frequency $\dot{\nu}_{\text{center}}$ and magnetic field strength \dot{B} on time scales comparable to the look-back times $t_{\text{LB},\nu}$ and $t_{\text{LB},B}$. As shown in figure 5.2.2, the corresponding measurements of ν_{center} and B show a linear trend, however deviate up to ± 20 Hz and ± 0.2 mGs from a linear fit respectively. Converting the latter value into a frequency using equation (3.1.4), leads to a detuning of about ± 11 Hz for the $(-1/2, -1/2)$ transition, as well as ± 56 Hz for the $(-1/2, -5/2)$ transition. These deviations lead to estimation errors of the offsets and drift rates, partially explaining the offsets and standard deviations of $\overline{\Delta}_{-1/2}$ and $\overline{\Delta}_{-5/2}$.

As indicated in figure 5.2.2 a higher order polynomial fit (e.g. third order as depicted) could reduce these residuals to below ± 10 Hz for the center frequency and to about ± 0.1 mGs for the magnetic field strength. Therefore, one can argue that more complex models of $\nu_{\text{center}}(t)$ and $B(t)$ are possible future extensions of this work. However, when increasing the complexity of the model, interpreting and monitoring the fit parameters becomes significantly more challenging. Thus, further investigation on the sources of the respective variations is necessary before extending the model to higher orders.

In order to quantify the achieved stability of the light field with respect to the $(-1/2, -1/2)$ and $(-1/2, -5/2)$ transition frequencies, the Allan deviation can be calculated from the data shown in figure 5.2.1 as discussed in section 3.1. As the data is split in intervals of one hundred measurements and the introduced Allan deviation requires constant time steps between data points, the detuning values of the first interval are used for the calculation of the Allan deviation with short averaging times < 100 s, and mean detuning values of the intervals are used for longer averaging times. The resulting Allan deviation is shown in figure 5.2.3 and is to be interpreted with respect to the $(-1/2, -1/2)$ and $(-1/2, -5/2)$ transition frequencies 411 042 153 376 142 (39) Hz and 411 042 012 176 088 (196) Hz respectively. The transition frequencies are calculated using equation (3.1.3) with the center frequency $\nu_{\text{center}} = 411\,042\,129\,776\,401.7$ (1.1) Hz [59] and the mean magnetic field $\overline{B} = 4.20351$ (7) Gs during the experiment.

Summarizing the results, it is possible to stabilize the frequency of a laser system using the adaptive Bayesian Ramsey spectroscopy algorithm, such that the difference between said frequency and the corresponding transition frequency is on the order of a few tens of Hertz. This leads to minimal Allan deviations (see figure 5.2.3) of $1.2(2) \cdot 10^{-14}$ with an averaging time of 100s for the $(-1/2, -1/2)$ transition and $7(1) \cdot 10^{-15}$ with an averaging time of 96s for the $(-1/2, -5/2)$ transition.¹ The increasing Allan deviations for larger averaging times are a result of the center frequency and magnetic field strength deviating from a linear trend as shown in figure 5.2.2. The choice of the look-back times $t_{\text{LB},\nu}$ and $t_{\text{LB},B}$ such as the approximation of the center frequency and magnetic field strength varying linearly within the corresponding look-back times are thereby crucial parameters and assumptions.

¹The corresponding minimal Allan deviations with respect to the $(-1/2, -1/2)$ and $(-1/2, -5/2)$ transition frequencies are 4.9(8) Hz and 2.9(4) Hz.

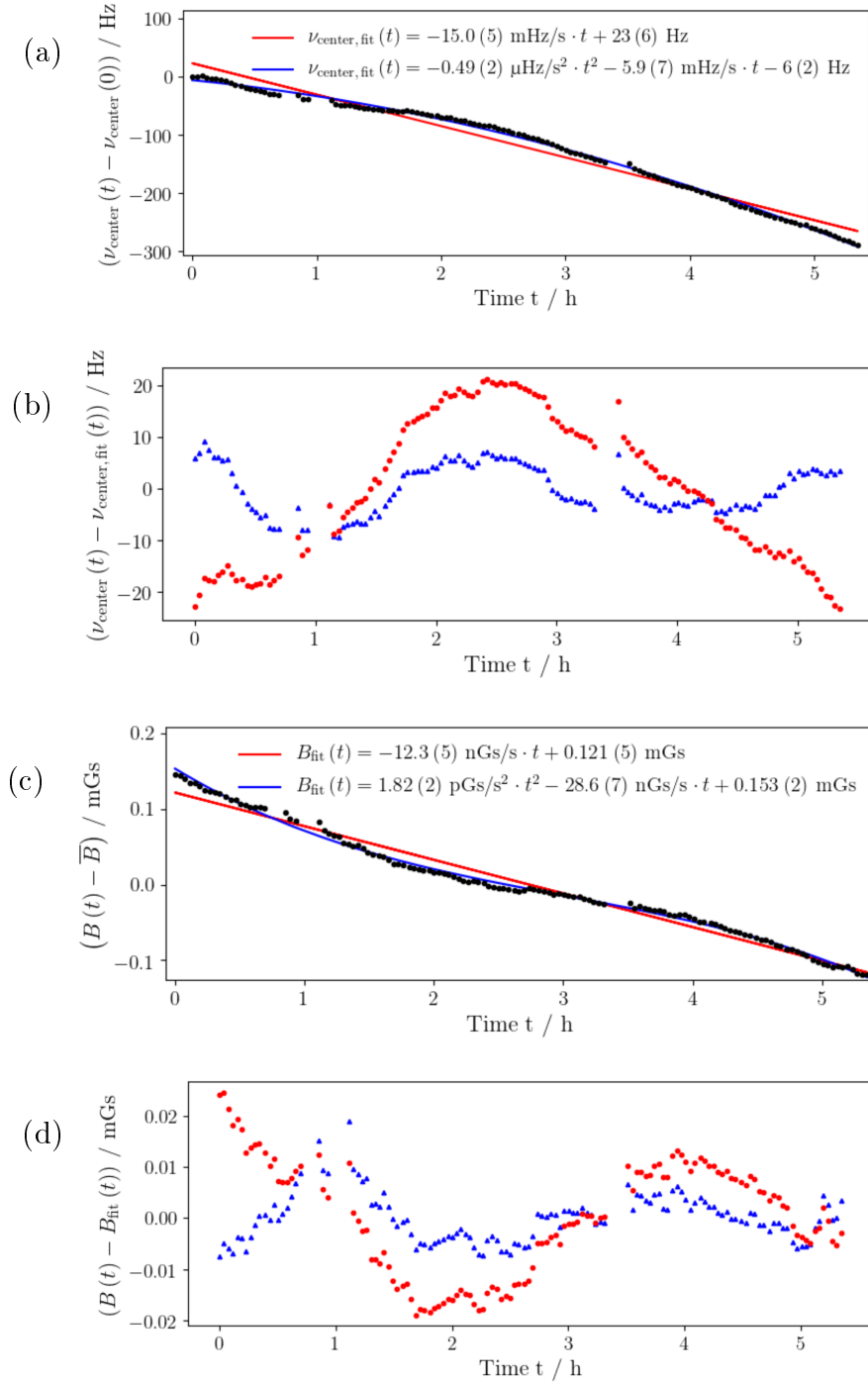


Figure 5.2.2: Measured center frequency ν_{center} and magnetic field strength B during the experiments resulting in the data shown in figure 5.2.1. (a) The differences of the measured values and the first measurement of the center frequency (black) are plotted against the time since said first measurement. A linear regression (red) is used to determine estimates for the drift and offset that are compensated. A third order polynomial fit (blue) is given for comparison. (b) The linear regression (red) as well as the polynomial fit are subtracted from the values to visualize how much the measured values deviate from a linear trend. (c) Similar to (a) the differences of the measured magnetic field strength values and the mean magnetic field strength $\bar{B} = 4.20351(7) \text{ Gs}$ (black) are plotted against time and fitted (red and blue). (d) Equivalent to (b).

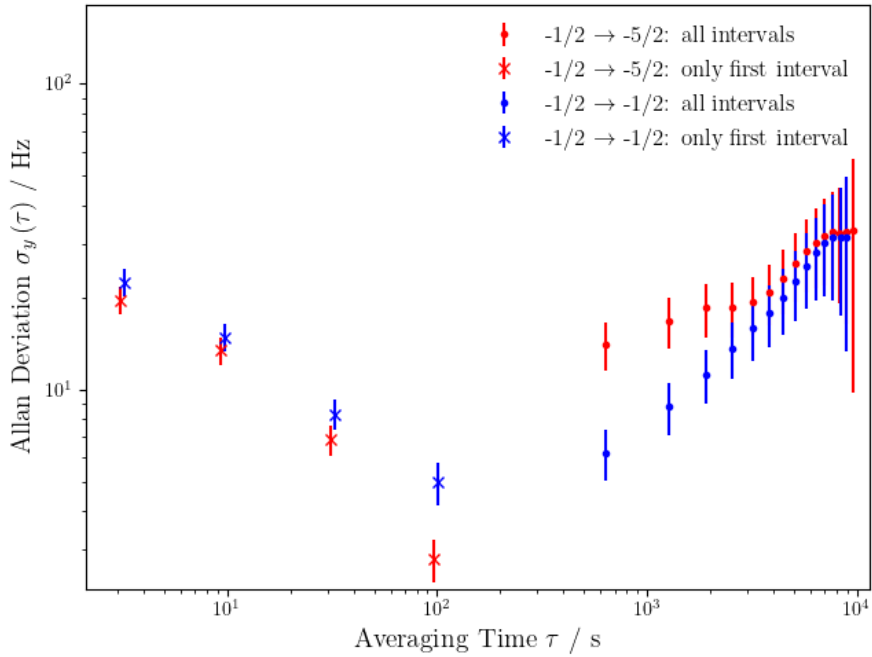


Figure 5.2.3: Allan deviation of the stabilized laser system with respect to the $(-1/2, -1/2)$ (blue) and $(-1/2, -5/2)$ (red) transition frequencies. The data points with averaging times below 100s are calculated from the first interval of the corresponding transition’s detuning in figure 5.2.1. The data points with larger averaging times are calculated from the mean detuning of each interval.

5.3 Variation of Drifts

The choice of the look-back times $t_{\text{LB},\nu}$ and $t_{\text{LB},B}$ is a crucial factor for the uncertainty of the frequency stabilization. Within this section, limits for the time span over which the drifts $\dot{\nu}_{\text{center}}$ and \dot{B} of the center frequency ν_{center} and the magnetic field B are constant are worked out by analyzing data of ν_{center} and B , as $t_{\text{LB},\nu}$ and $t_{\text{LB},B}$ depend on the variation of $\dot{\nu}_{\text{center}}$ and \dot{B} . First, short-term variations on the order of hours are discussed, finding the limits of the look-back times. Long-term variations in the order of months are discussed afterwards.

Short-Term Variations

Figure 5.3.1 shows measured values for ν_{center} and B during a calibration with the adaptive Bayesian Ramsey spectroscopy mode, performing spectroscopic measurements every 2.5 minutes. Within the displayed period of ~ 4.5 hours, ν_{center} is detuned by about 400Hz and shows a linear trend. In order to characterize this linear trend with respect to a look-back time $t_{\text{LB},\nu}$ of one hour, the data is split into overlapping intervals with each interval spanning over one hour. Consecutively, a linear fit is performed within each interval. The mean deviation of each interval’s data points from the corresponding linear fit is displayed in figure 5.3.2, and fluctuates between 5.5Hz and 21.5Hz. The deviations from the linear trend can be a result of residual temperature fluctuations, and vibrations. Therefore, depending on the desired accuracy

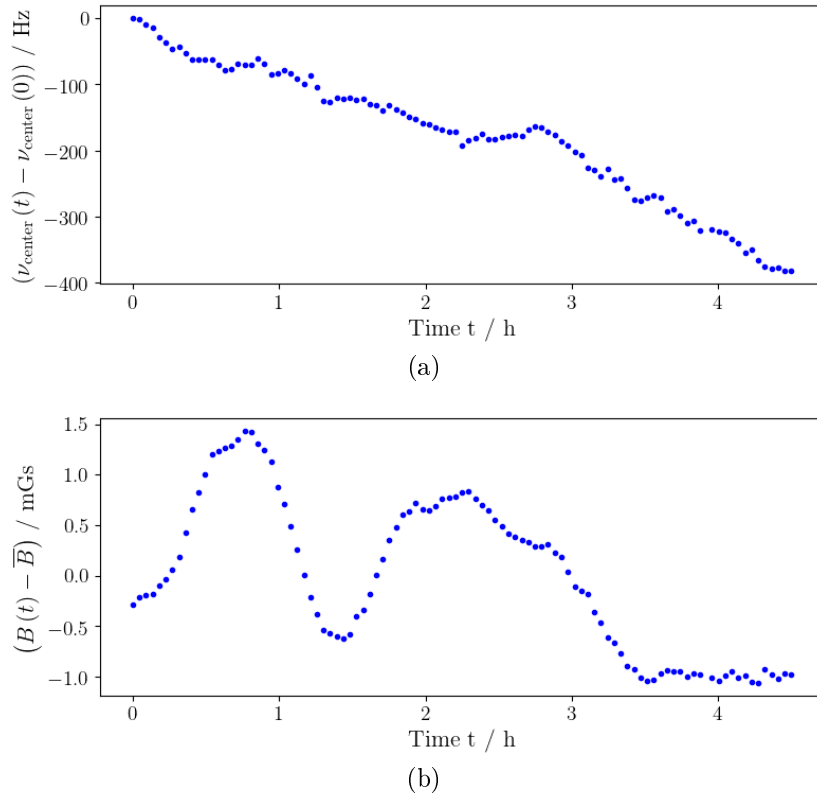


Figure 5.3.1: Short-term variations of the center frequency ν_{center} and magnetic field strength B over the course of several hours. (a) The detuning between the first measurement of ν_{center} at time $t = 0$ and the subsequent ones is plotted against the time t . The data shows a linear trend except for deviations in the order of a few tens of Hertz. (b) The difference between the measured magnetic field strength $B(t)$ at a given time t and the mean value \bar{B} of B within the given interval is plotted against t . Variations of \dot{B} happen drastically and on time scales below an hour.

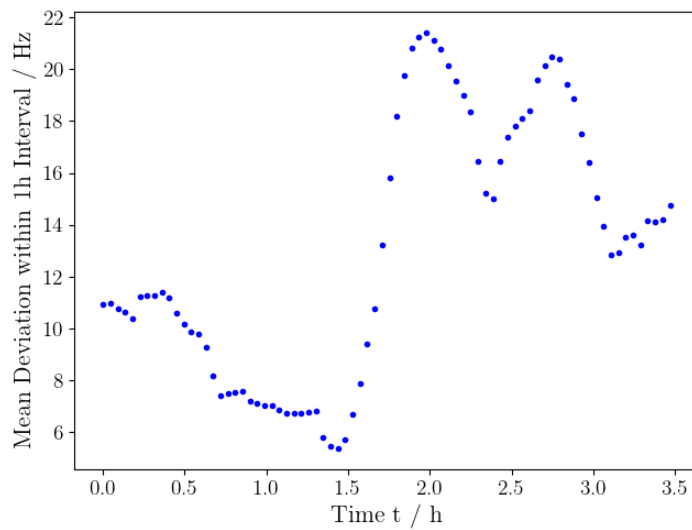


Figure 5.3.2: Mean deviation from a linear trend within one hour intervals against the starting time of each interval.

and the time between spectroscopic updates, limiting $t_{\text{LB},\nu}$ to be in the order of one hour is reasonable.

As shown in figure 5.3.1b, the measured magnetic field strength values do not show a linear trend over the course of the observed time scales, but fluctuate around a mean value of $\overline{B} = 4.1769(8)$ Gs. Using equation (3.1.4), the maximal measured deviation from \overline{B} of about 1.5 Gs translates to a -4.2 kHz Zeeman shift of the $(-1/2, -5/2)$ transition frequency, which is two orders of magnitude larger than the deviations of the center frequency from its linear trend. Possible reasons for the variations of the magnetic field strength at the position of the ions are fluctuations in the current of the magnetic field coils generating the desired Zeeman splitting of the $4^2\text{S}_{1/2}$ and $3^2\text{D}_{5/2}$ states, magnetic fields generated by neighboring experiments, or magnetic fields generated by other electronics within the laboratory. As the look-back time $t_{\text{LB},B}$ has to be well below the time scales of these fluctuations, it can be necessary to limit $t_{\text{LB},B}$ to be in the order of ten minutes, depending on the present conditions.

Long-Term Variations

Measuring ν_{center} and B over the course of about 200 days, results in the graphs depicted in figure 5.3.3, showing similar features to the short-term variations discussed above. Again, a linear trend of ν_{center} is observable, leading to a constant drift of $\dot{\nu}_{\text{center}} = -19.485(5)$ mHz/s . The outliers in figure 5.3.3a can be associated with days where work has been performed on the laser system or the experimental setup. The measured constant drift of $-19.485(5)$ mHz/s is about one order of magnitude lower than the previously mentioned drift of 370 mHz/s [42] that has been measured on a similar system.

Figure 5.3.3b shows that B is fluctuating on long time scales and does not show any obvious regularities or trends. As discussed above, these fluctuations can have different reasons, magnitudes and time scales, and are therefore not feasibly predictable. However, the offsets and drifts can be compensated for within the typical time scales of an experiment in the order of hours, as shown in section 5.2.

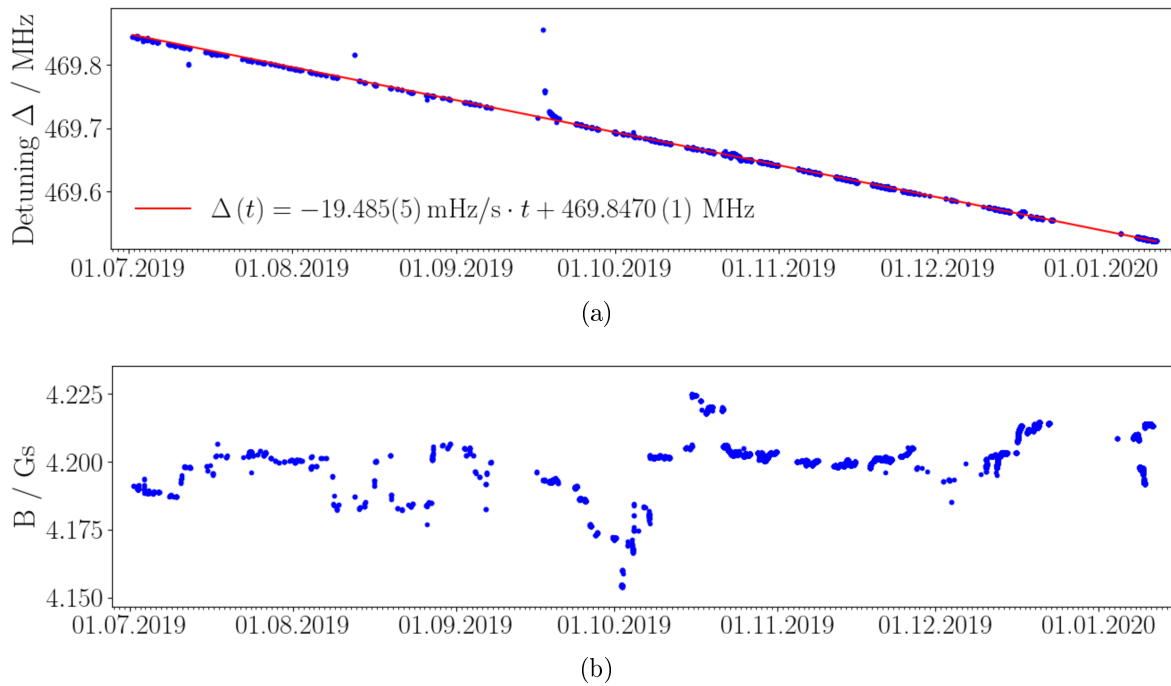


Figure 5.3.3: Long-term variations of the center frequency ν_{center} and magnetic field strength B over the course of six months. (a) The detuning between the measured values for ν_{center} and the laser system operating at a wavelength of 729 nm is plotted against the corresponding date of measurement. A linear trend is observable, with outliers being coincident with days where work has been performed on the experimental setup. (b) The measured values of B plotted against the corresponding measurement date do not show any obvious trends or regularities.

Chapter 6

Simplified Quantum Computer Control

Executing quantum algorithms on a quantum computer, requires some level of automation to focus on the quantum algorithm, instead of e.g. continuous re-calibration of the system. Furthermore, it is necessary to have a quantum programming language available. Such a language needs to translate high-level operations into laser pulses with individual frequencies, phases, durations and intensities. Here, a quantum computer control framework is presented, in which sub-routines of the quantum computer experiment can be automated, and standardized pulse description languages can be defined. The software design of this framework has to be modular to be agile with respect to future requirements, and to allow for automation of the individual modules.

The experiment control framework is given by the Quantum Control Program (QCP). The QCP is a computer program written in the Python programming language that controls all the hardware required for the given experiment. It is noteworthy that the program, automating the continuous re-calibration of the laser system operating at a wavelength of 729 nm, is included in the QCP, can however also be used independently with reasonably little effort. Two quantum algorithm description languages are discussed, both being implemented in the QCP, evaluating their advantages and disadvantages for specifying and executing quantum algorithms. Last but not least the QCP's feature of allowing remote control of the quantum computer is discussed with the example of the Bernstein-Vazirani algorithm [60] which has been executed on the quantum computer from a remote location [61].

6.1 Quantum Control Program

The Quantum Control Program (QCP) is a modular program, designed mostly by Philipp Schindler and Michael Meth. The contributions of this thesis to the QCP are the implementation of the frequency stabilizing program as discussed before, as well as the integration of two quantum algorithm description languages that will be discussed below. The QCP is written in the programming language Python¹, and controls all hardware required for the given quantum computer experiment. The main

¹version 3.7. as of writing this thesis

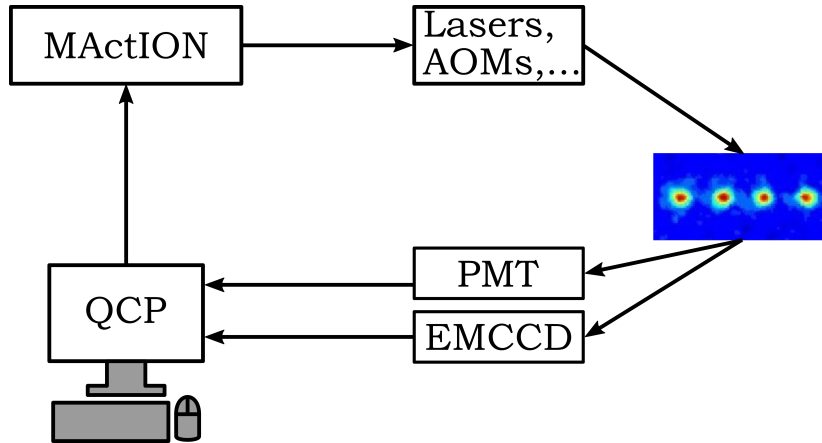


Figure 6.1.1: Experiment control system. The Quantum Control Program (QCP) controls the MActION system, which in turn sends electrical signals to the individual parts of the experiment. The ion fluorescence data taken by the PMT and the EMCCD camera is interpreted by the QCP.

parts of the experimental control system consist of the ion trap quantum computer, with all associated laser systems as elaborated on in chapter 2, a control hardware called MActION system [62], generating the electrical pulses to trigger and tune the individual parts of the experiment, and a computer running the QCP, controlling the MActION system and interpreting the ion fluorescence data that is returned by the EMCCD camera or the photo multiplier tube (PMT). A schematic depiction of this setup can be found in figure 6.1.1. The MActION system, being programmed in the C/C++ programming language, is a controller that is developed by the Institut für Quantenelektronik of the ETH Zürich and generates phase coherent RF signals via direct digital synthesis (DDS), as well as digital outputs via transistor-transistor logic (TTL). A camera as well as a PMT return the results of fluorescence measurements to the computer running the QCP.

The modular software design of the QCP makes it possible to exchange every hard- and software part of this setup or to extend it with new modules with comparably little effort. A screenshot of the QCP’s graphical user interface (GUI) can be found in figure 6.1.2. This modular design also makes it possible to write automation modules. One of these automation modules is the frequency stabilizing program, being a central part of this thesis. From within the QCP, such as from its GUI, it is possible to set the initial parameters of the frequency stabilizing program, and to observe the measured spectroscopic updates and derived drifts. It is also possible to tune the look-back times $t_{LB,\nu}$ and $t_{LB,B}$, such as the time between spectroscopic updates, as well as to manually remove outliers of the measured center frequency or magnetic field strength values. Other automation modules include:

- Doppler cooling
- Rabi frequency measurements
- Ion temperature measurements
- Complex quantum state generation and subsequent experiments.

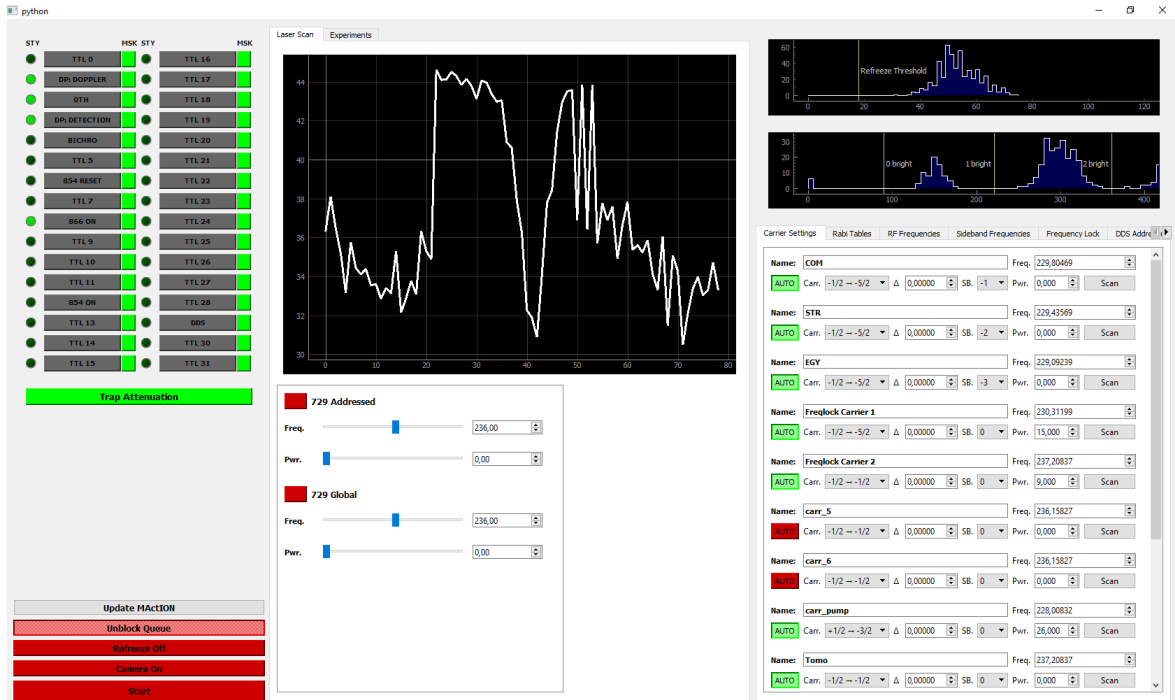


Figure 6.1.2: Screenshot of the QCP's GUI. The desired information can be displayed, while experimental parameters like i.e. the frequency of a used laser can be set. Furthermore, experiments can be conducted by starting user-defined sequences or by measuring mean excitations while scanning a parameter over a desired range.

Most of these modules have in common, that from the perspective of a user, only few button clicks are required to tune and scan parameters. For example as shown in figure 6.1.3, when submitting a parameter scan of the duration of a light pulse with a given frequency and intensity, the measured mean excitation that is plotted by the QCP's GUI represents Rabi oscillations of the trapped ions, which can then be analyzed by a tool of choice.

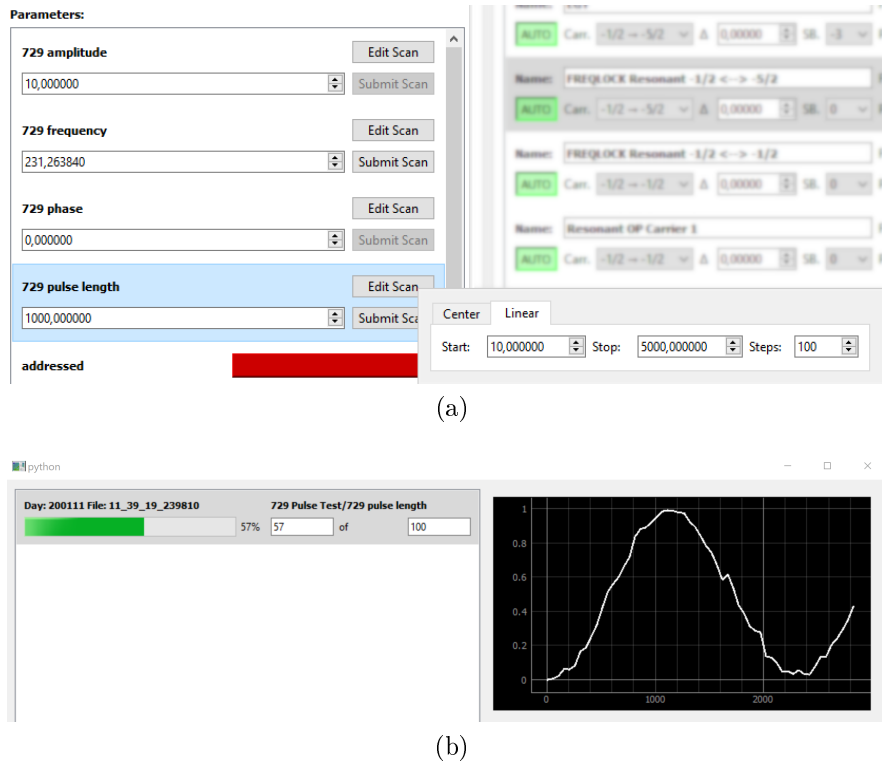


Figure 6.1.3: Screenshots of the QCP’s GUI performing Rabi oscillations. (a) The desired parameters can be set via the numerical input fields on the left. A parameter can be scanned using the “Edit Scan” and “Submit Scan” buttons. (b) The measurement results of the submitted parameter scan are then plotted as mean excitation against the parameter value. In the given case, Rabi oscillations are shown with the scanned parameter being the light pulse duration in microseconds.

6.2 Quantum Programming Languages

As a classical computer is used to control the experimental parameters and to interpret the results, it is necessary to describe quantum algorithms as well as their results in a classical programming language, to perform them on the given quantum computer experiment. Furthermore, it is desired that an end-user does not have to care about the particular architecture of a quantum computer or the actual implementation of the quantum algorithm. Such a level of abstraction can only be achieved, if all layers between the actual quantum part of the quantum computer and the quantum algorithm are identified. In figure 6.2.1, these layers are depicted as introduced in reference [63]. In order to identify the terms introduced by the authors of reference [63]:

- The quantum chip corresponds to the qubits encoded in optical transitions of the ions inside a linear ion crystal of the experimental setup.
- The quantum-classical interface is given by the lasers controlling the state of the qubits, and the camera and PMT measuring it after an experiment.
- The quantum execution (QEX) block corresponds to the generation of phase coherent pulses.

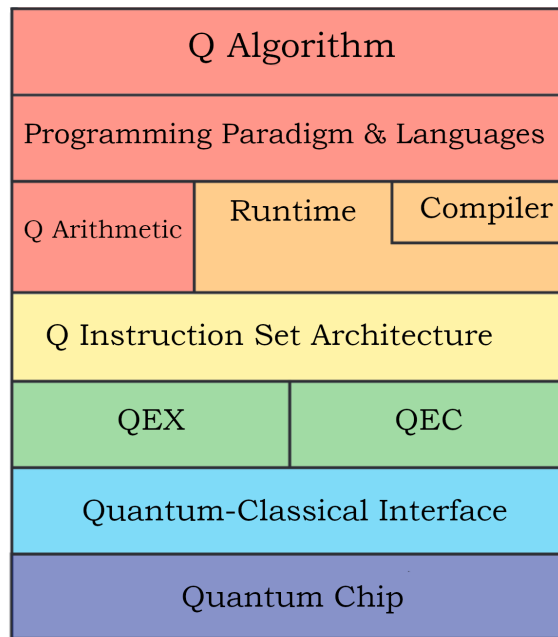


Figure 6.2.1: Layers of a quantum computer. Inspired by figure 3 of reference [63], the layers between the definition of a quantum algorithm (top) and the physical implementation on a corresponding quantum chip (bottom) are displayed. A detailed description of these layers can be found in section 6.2.

- The quantum error correction (QEC) block is not relevant for the current system, however theoretically takes methods into account to protect the encoded information from the environment.
- The quantum instruction set architecture (QISA) describes the set of quantum gate operations that can be performed on the qubits.
- The layer above the QISA is the interface to the software describing the quantum algorithm, by converting the specified quantum gates into the ones that are exposed by the QISA.
- The two uppermost layers show the quantum algorithm that should be executed, as well as its description written in a given programming language.

There are many paradigms and languages in which quantum algorithms can be described, like e.g. natural languages including formulas and mathematics. For a computer however, natural languages are typically challenging to interpret, making the creation of a corresponding compiler infeasible. Therefore, it is desired to find a language for which either such a compiler already exists or can be created, without increasing the complexity of the quantum algorithm's description. In other words, both the end-user and the computer have to be able to read the language and understand the algorithm with reasonably little effort. Within the scope of this thesis, two quantum algorithm description languages have been implemented and tested. Both languages, the JavaScript Object Notation (JSON) based OpenPulse [64] developed by the Inter-

national Business Machines Corporation (IBM), as well as the Python based Cirq [65] developed by Google LLC are going to be elaborated on below.

OpenPulse

OpenPulse is a quantum algorithm description language developed by IBM. The JSON format, a textual description of data as specified by reference [66], is the basis of OpenPulse. Typically JSON objects are used to send data between processes or computers and are often found in web-development, as the original idea of a JSON object is to be the main communication format of the (web-)programming language JavaScript.

A JSON object is encased with curly brackets and contains so called key-value pairs, where the key is used to label the data that is stored in the value. The key and value are thereby separated by a colon, where the first entry is always the key. Key-value pairs are separated from each other by commas. The key has to be a string, indicated with double quotes, whereas the value can be of a different data type, like i.e. a number, or a list, the latter being encased with rectangular brackets. Furthermore, it is possible to nest JSON objects, i.e. using a JSON object as a value. An exemplary JSON object showing all aforementioned features can be found in listing 6.1.

OpenPulse uses the JSON format to define sequences of quantum gates, as well as their parameters. The compiler then sequentially reads the JSON objects that are submitted and translates them into the corresponding set of quantum gates exposed by the Quantum Instruction Set Architecture (QISA) as described above. An OpenPulse description of a Ramsey sequence on two qubits can be found in listing 6.2. Thereby, the header gives information about the experiment, in this case the name of the sequence, and the instructions key labels the sequence of quantum gates, stored as a list of JSON objects. The items of this list are sequentially interpreted by the compiler, and in this case executed one after the other. Each of these quantum gate objects, has a name the compiler can interpret and translate to quantum gates that are exposed by the QISA. The qubits list then indicates on which qubits the operation has to be performed on, and the params key specifies the parameters for the corresponding operation. In the case shown in listing 6.2, the instruction

```
4 {"name": "X", "qubits": [1, 2], "params": [0.5]},
```

Listing 6.1: Example of the JSON format. A JSON object is encased with curly brackets. The object's data is stored as key-value pairs. Nesting JSON objects is possible.

```
1 {
2   "key_1": 123.456,
3   "key_2": "value_2",
4   "key_3": ["value_3.1", "value_3.2"],
5   "key_4": {
6     "key_5": "value_5"
7   }
8 }
```

corresponds to a 90° rotation around the x-axis of the Bloch sphere of the qubits labeled one and two, i.e. a $\pi/2$ -pulse. The second instruction

```
5 {"name": "wait", "qubits": [], "params": [100]},
```

corresponds to a waiting time of $\tau = 100\ \mu\text{s}$, and the third one

```
6 {"name": "X", "qubits": [1, 2], "params": [0.5]}
```

to a $\pi/2$ -pulse again. As a remark, the example shown in listing 6.2 is a simplified OpenPulse sequence to explain its principle. For a thorough explanation of the whole OpenPulse protocol, the reader is referred to [64].

The advantages and disadvantages of OpenPulse are inherently linked to the underlying JSON format. On the one hand such textual data formats lead to a straight forward implementation of an interpreter, by reading and executing the specified instructions one after the other. Furthermore, the JSON format is well suited for communication between processors, as it has been developed with that intention. Therefore, an OpenPulse file can be sent from the QCP to the MActION system and be interpreted by the latter, directly translating the instructions to RF signals.

Two major disadvantages of OpenPulse arise when thoroughly investigating its specifications. As OpenPulse is developed with having quantum computers using superconducting qubits in mind, the rigorous definition does not fit an ion trap quantum computer architecture properly without adaptations. On the one hand, as JSON is a description language and not a programming language, OpenPulse lacks some functionality like i.e. scanning parameters in a straight forward manner, or defining global parameters to make a quantum algorithm more readable. On the other hand, some functionalities and parameters are exposed by OpenPulse that are cumbersome to implement like e.g. the fact that OpenPulse requires the quantum computer to expose a coupling map, defining which qubits can interact with each other, where in the given architecture all qubits can be coupled with one another arbitrarily. Both these problems lead to a rather complex description of the desired quantum algorithm, where an end-user has to have a thorough understanding of the actual implementation of the corresponding quantum gates.

Listing 6.2: An OpenPulse Ramsey sequence. The header gives information of the algorithm, while the instructions sequentially specify the quantum gates that have to be performed.

```
1 {
2   "header": {"name": "Ramsey Sequence"},
3   "instructions": [
4     {"name": "X", "qubits": [1, 2], "params": [0.5]},
5     {"name": "wait", "qubits": [], "params": [100]},
6     {"name": "X", "qubits": [1, 2], "params": [0.5]}
7   ]
8 }
```

Cirq

The quantum algorithm programming language Cirq, developed by Google LLC, is based on the Python programming language, which is the same language in which the QCP is written in. Cirq is a Python library that defines quantum gates in an object oriented way. The user specifies the desired number of qubits such as their architecture, followed by the quantum gates that are needed for the quantum algorithm. Then a circuit object is generated and filled up with the gates corresponding to the desired sequence. An example for a Ramsey sequence written in Cirq can be found in listing 6.3. Similarly to the OpenPulse example shown in listing 6.2, the $\pi/2$ -pulses

```
7 pi_half = cirq.X(qubits)**0.5
```

are specified as 90° rotations around the x-axis of the Bloch sphere of the given qubits, and

```
8 wait = cirq.WaitGate(cirq.Duration(micros=100))
```

defines a $\tau = 100 \mu\text{s}$ wait gate. After appending all gates of the quantum algorithm to the circuit object, it is possible to either display the circuit graphically, or to send the object to an interpreter that executes or simulates it.

Having Python as the basis for Cirq leads to many advantages such as a comparatively high readability of the algorithm, and the possibility to define specific objects in order to reuse them, as is done in listing 6.3 with the $\pi/2$ -pulses. Furthermore, it is possible to create loops, filling the circuit object in an automated manner with e.g. the same gates but different parameters, effectively allowing a user to perform a scan over some parameter. The created circuit object can then natively be interpreted by the QCP as both are written in Python, or parsed into a text based language like OpenPulse. A disadvantage of Cirq is, that it is still in development phase resulting in unstable syntax.

Listing 6.3: Example of a Cirq Ramsey sequence. The shown Python code snippet imports the cirq library and defines the qubits and quantum gates. The circuit object is then filled with the respective quantum gates and can be sent to a compiler to be executed.

```
1 import cirq
2
3 # define the qubits
4 qubits = [cirq.LineQubit(i) for i in range(2)]
5
6 # define all necessary gates
7 pi_half = cirq.X(qubits)**0.5
8 wait = cirq.WaitGate(cirq.Duration(micros=100))
9
10 # append the gates to a circuit object
11 circuit = cirq.Circuit()
12 circuit.append(pi_half)
13 circuit.append(wait)
14 circuit.append(pi_half)
15
16 # the circuit object can then be sent to a compiler
```

PInT and PySeq

Comparing OpenPulse and Cirq, the former has a rigorous definition that does not perfectly fit ion trap quantum computer architectures and the latter is still in its development phase. Combining the best of both worlds, it has been decided to use a Python based quantum programming language as interface between the end-user and the QCP, as well as a JSON based description language for the communication between the QCP and the MActION system, with the latter interpreting the JSON objects and executing them.

Using a JSON based language for the internal communication has the advantage that the JSON objects can directly be translated into RF signals generating laser pulses. The disadvantage of OpenPulse's rigorous definition not matching the given architecture is circumvented by creating a custom description language that shares the basic principles and concepts with OpenPulse. This language is called Pulse Instruction Text (PInT) and is intended to simplify the internal communication between the QCP and the MActION system. An exemplary PInT object can be found in listing 6.4.

The PInT uses the nesting features of JSON one level deeper than OpenPulse, by describing the parameters more explicitly. Furthermore, flags are added that can be used to interpret the parameters. Both these features make the text longer, however more readable from the perspective of a programmer debugging the communication between the QCP and the MActION system. Thus, PInT can be seen as a simplified version of OpenPulse that has been adapted to ion trap experiments.

The parameters and flags that are available depend on the desired quantum gate. For a unitary rotation on the Bloch sphere, the duration of the corresponding light pulse, the phase and the qubits that are addressed can be specified. Moreover, it is possible to address the two qubits with different phases and to vary the frequency of the light pulses. The latter is done by modifying so called carrier objects that are specified on the MActION system and referenced by the *carrier_idx* parameter. In contrast to OpenPulse, where the whole protocol includes answers for requests, PInT is only used to send instructions to the MActION system. The results are analyzed by the QCP without any further programming overhead.

Increasing the readability for an end-user, a Python based programming language is chosen as user interface. Avoiding the interface to break when Cirq is updated to newer versions, the custom language Python-Sequence (PySeq) is created. PySeq thereby uses similar syntax and principles as Cirq and is therefore not discussed in more detail. An example for a Ramsey sequence defined via PySeq can be found in listing 6.5. A parsing between the two languages of Cirq and PySeq is straight forward, allowing an end-user to use either Cirq or PySeq to submit a quantum algorithm to the QCP and receiving its results in the desired format. Furthermore, a parser between OpenPulse and PySeq has been developed, allowing for some support of OpenPulse as quantum algorithm description language as well. All in all, the implementation of PInT and PySeq profits from the advantages of OpenPulse and Cirq, while circumventing some of their disadvantages, having a high readability when defining quantum algorithms, while maintaining a straight forward way to implement an interpreter that executes the quantum gates the quantum algorithm consists of.

Listing 6.4: A PInT Ramsey sequence. The PInT is based on OpenPulse, however uses a more explicit description of the parameters, while removing overhead by reducing the overall protocol.

```
1 {
2   "header": {"name": "Ramsey Sequence"},
3   "instructions": [
4     {"name": "U",
5      "parameters": {
6        "carrier_idx": 1,
7        "duration": 0.5,
8        "qubits": [1, 2],
9        "phase": 0.0,
10       "addr_phases": []
11      },
12     "flags": {
13       "is_global": false,
14       "is_time_pi": true
15     }
16   },
17   {"name": "wait",
18    "parameters": {
19      "duration": 100,
20    },
21    "flags": {
22      "is_global": true,
23      "is_time_pi": false
24    }
25   },
26   {"name": "U",
27    "parameters": {
28      "carrier_idx": 1,
29      "duration": 0.5,
30      "qubits": [1, 2],
31      "phase": 0.0,
32      "addr_phases": []
33    },
34    "flags": {
35      "is_global": false,
36      "is_time_pi": true
37    }
38   },
39 ]
40 }
```

Listing 6.5: Example of a PySeq Ramsey sequence. The shown Python code snippet is the PySeq equivalent of the Cirq code shown in listing 6.3.

```
1 import pyseq
2
3 # define the qubits
4 qubits = range(2)
5
6 # define all necessary gates
7 pi_half = ResonantOp(phi=0, theta=0.5)
8 wait = WaitOp(100)
9
10 # append the gates to a list
11 seq_list = []
12 seq_list.append(pi_half)
13 seq_list.append(wait)
14 seq_list.append(pi_half)
15 qseq = QSequence(seq_list)
16
17 # the sequence can then be sent to a compiler
18 rs = RunSequence([qseq])
```

6.3 Remote Access

Representational State Transfer (REST) application programming interfaces (APIs) are a standardized way for web services to allow users the access and manipulation of data, and therefore build the backbone of the internet. As quantum algorithms can be submitted to the QCP using the description languages described in section 6.2, a REST-API is implemented, allowing the submission of quantum algorithms from remote locations [61]. This has the major benefits of simplifying cooperations with collaborators all over the world, as well as the ability to offer the computation of quantum algorithms on the given quantum computer as a service. Without going into detail, a web service that implements a REST-API offers a standardized interface to submit commands and receive responses. Within the implemented interface it is possible to submit quantum algorithms to the QCP using the quantum algorithm description language Cirq. In order to ensure security, i.e. preventing unauthorized access to the QCP, the OAuth2.0 protocol [67, 68] is used. Within this protocol, the web service implementing the QCP's REST-API redirects a user to a server, where the user has to log in with their account and grant the application access to some personal data like i.e. their email address. An access token is then sent to the application with which the user information can be accessed by the application. In the case of the QCP's web service, a user has to submit a valid access token together with the desired quantum algorithm. If the web service can access the required personal data of the user, and the user is allowed to run quantum algorithms, as specified by the QCP's private database, the submission is accepted and the quantum algorithm is executed. Using this protocol as authentication has the major advantage of outsourcing most security related issues to large companies like i.e. Google LLC, while still having control over which accounts are granted or denied access to the quantum computer.

The proof of principle experiment referred to by reference [61], is the remote execution of the Bernstein-Vazirani quantum algorithm [60], utilizing the implemented REST-API. The quantum algorithm is implemented in Cirq according to the description in section 6.2 and is equivalent to the circuit specified in reference [69]. Code snippets describing the submission of the quantum algorithm can be found in listing 6.6. First, the circuit has to be specified and parsed into a JSON format, to simplify the actual submission of the circuit. Then the user has to send the circuit together with a valid OAuth2.0 access token to the Uniform Resource Locator (URL) of the QCP's web service, using the REST-API request *put*. As an answer of this request, the user obtains a JSON object containing information on the submitted quantum algorithm, such as its ID or its status. The status of the submission thereby tells the user if the processes is waiting to be executed (i.e. if it is *queued*), has been aborted, has failed, or if it has finished successfully. With subsequent *put* requests, this status can be queried, and as soon as there is information available, the user obtains said information with the corresponding JSON object.

Listing 6.6: Code snippets describing the remote submission of quantum algorithms. The shown code gives an overview of the remote access protocol, omitting some details using ellipses (...) instead. A description of the protocol can be found in section 6.3

```
1 import cirq
2 import json
3 from requests import put
4
5 # define the Bernstein-Vazirani circuit as described in
6 # previous examples
7 circuit = cirq.Circuit()
8 circuit.append([...])
9
10 # parse the circuit to a JSON format
11 circuit_json = json.dumps(...)
12
13 # send the circuit to the web service
14 access_token = "insert-oauth2.0-access-token-here"
15 data = put('http://URL-of-web-service',
16           data={'access_token':access_token,
17                 'data':circuit_json,
18                 ...}).json()
19
20 # query the status to receive the result
21 while data['status'] is "queued":
22     data = put('http://URL-of-web-service',
23               data={'access_token':access_token,
24                     'id':data['id']}).json()
25
26 # print the result
27 print(data)
```

Chapter 7

Summary and Outlook

Within this thesis, a program has been implemented that stabilizes the frequency of the laser system used for qubit operations in an automated manner. The program compensates for drifts and offsets resulting from changes to the length of the cavity the laser is stabilized to, as well as from variations of the magnetic field at the position of the trapped ions. The program can be used in either of two modes. The initial mode uses Rabi spectroscopy with a subsequent least squares algorithm analyzing the data. The second mode, being optimized for a continuous re-calibration of the system, and for increased accuracy and stability, utilizes Ramsey spectroscopy as well as an adaptive Bayesian algorithm for the subsequent data analysis.

It is shown that by using said program in its initial mode the uncertainty of a transition frequency can be reduced to a few KiloHertz. The resulting uncertainty is shown to be small enough to initialize the adaptive Bayesian Ramsey spectroscopy mode, which can then be used to tune the laser system more precisely. The main advantages of the Rabi spectroscopy mode are its ability to cope with limited knowledge, as well as its straight forward initialization. The main disadvantage is the time it takes for the Rabi spectroscopy mode to gather enough data required for a confident analysis, reducing the duty cycle of the quantum computer experiment.

The adaptive Bayesian Ramsey spectroscopy mode of the frequency stabilizing program uses Bayesian inference to analyze the results of Ramsey experiments as well as to adaptively calculate the parameters for the most informative experiments. This simultaneously increases the accuracy of the spectroscopic results while reducing the number of measurements required for the data analysis. Spectroscopic updates conducted by the frequency stabilizing program in its adaptive Bayesian Ramsey spectroscopy mode thereby take a few seconds to be completed, allowing the system to be continuously re-calibrated without leading to a significant reduction of the quantum computer experiment's duty cycle. The uncertainty resulting from a frequency stabilization by the adaptive Bayesian Ramsey spectroscopy mode is estimated to be in the order of a few tens of Hertz. The stability of the laser system calibrated by the adaptive Bayesian Ramsey spectroscopy algorithm reaches a minimal Allan deviation of $7 \cdot 10^{-15}$ for an averaging time of 96 s. This corresponds to an Allan deviation of 2.9 (4) Hz with respect to the $(-1/2, -5/2)$ transition frequency. A crucial factor for the stability is given by the linear regression predicting the current values of the center frequency ν_{center} and the magnetic field strength B , neglecting short-term variations of the corresponding

drifts $\dot{\nu}_{\text{center}}$ and \dot{B} . Tuneable look-back times $t_{\text{LB},\nu}$ and $t_{\text{LB},B}$ have been introduced to counter this problem. The choice of the look-back times depends on the given conditions in the laboratory, with the center frequency typically showing linear trends over the time scale of hours and the magnetic field strength fluctuating irregularly on these timescales. A possible future extension of this work is given by further investigating these deviations from a linear trend in order to utilize higher order model functions that predict the current values of ν_{center} and B .

In order to implement the adaptive Bayesian Ramsey spectroscopy mode of the frequency stabilizing program, a Bayesian framework, as well as quantum algorithm description languages have been implemented. The latter being intended to allow a straight forward description of the Ramsey experiments, which is necessary to facilitate a low-key communication between the available soft- and hardware, while maintaining human readability. With the introduction of quantum algorithm description languages however, the opportunity has been taken to generate an interface using already established quantum programming languages with Google's Cirq and IBM's OpenPulse. Furthermore, allowing for remote access using these languages, while ensuring security by adhering to the OAuth2.0 protocol, the communication and cooperation with collaborators around the world has been simplified. A possible improvement of this interface can be achieved by including other quantum programming languages like i.e. pyAQASM which is developed by Atos SE [70].

The Bayesian framework is implemented in a modular way such that it can be used to optimize and automate other subroutines of the quantum computer experiment. As hinted at in section 5.2, to initialize the adaptive Bayesian Ramsey spectroscopy mode, the $\pi/2$ -time $\tau_{\pi/2}$ as well as the phase coherence time T_2 have to be measured. Both these measurements can be automated using Bayesian inference to analyze the results of the corresponding Rabi or Ramsey experiments and to adaptively calculate the parameters for the most informative next experiment. Furthermore, experiments to find the optimal parameters of high fidelity Mølmer-Sørensen gates [71], or other quantum gates can be automated using a Bayesian framework. Both an automated Bayesian $\tau_{\pi/2}$ measurement, as well as an automated Bayesian tune-up of high fidelity Mølmer-Sørensen gates are currently being worked on, as integrating such Bayesian automation schemes helps to increase the performance while reducing the time spent for the corresponding sub-routines.

Disclaimer

This thesis and all related work results from a cooperation between the Universität Innsbruck and the Alpine Quantum Technologies GmbH (AQT). Parts of the programs used in this thesis have been developed and written while the author has been employed by AQT. Both partners of this cooperation are allowed to use, modify and profit from the programs and applications created within the scope of this work.

Bibliography

- [1] Konrad Zuse. *Der Computer - Mein Lebenswerk*, volume 5. Springer Berlin Heidelberg, 2010.
- [2] Curtis Struck. Simulations of collisions between two gas-rich galaxy disks with heating and cooling. *The Astrophysical Journal Supplement Series*, 113(2):269–309, dec 1997.
- [3] Mariusz Bojarski, Davide Del Testa, Daniel Dworakowski, Bernhard Firner, Beat Flepp, Praseoon Goyal, Lawrence D. Jackel, Mathew Monfort, Urs Muller, Jiakai Zhang, Xin Zhang, Jake Zhao, and Karol Zieba. End to end learning for self-driving cars, 2016.
- [4] Berry M. Leiner, Vinton G. Cerf, David D. Clark, Robert E. Kahn, Leonard Kleinrock, Daniel C. Lynch, Jon Postel, Larry G. Roberts, and Stephen Wolff. Brief History of the Internet. Internet Society, 1997.
- [5] Gordon E. Moore. Cramming more components onto integrated circuits. *Electronics*, 38(8), April 1965.
- [6] G. Yeric. Moore’s law at 50: Are we planning for retirement? In *2015 IEEE International Electron Devices Meeting (IEDM)*, pages 1.1.1–1.1.8, Dec 2015.
- [7] L. Eeckhout. Is Moore’s Law Slowing Down? What’s Next? *IEEE Micro*, 37(04):4–5, jul 2017.
- [8] H. Häffner, C.F. Roos, and R. Blatt. Quantum computing with trapped ions. *Physics Reports*, 469(4):155 – 203, 2008.
- [9] P. W. Shor. Algorithms for quantum computation: discrete logarithms and factoring. In *Proceedings 35th Annual Symposium on Foundations of Computer Science*, pages 124–134, Nov 1994.
- [10] Lov K. Grover. A fast quantum mechanical algorithm for database search. In *Proceedings of the Twenty-eighth Annual ACM Symposium on Theory of Computing, STOC ’96*, pages 212–219, New York, NY, USA, 1996. ACM.
- [11] Michael A. Nielsen and Isaac L. Chuang. *Quantum Computation and Quantum Information*. Cambridge University Press, 2010.

- [12] D. J. Wineland, C. Monroe, W. M. Itano, D. Leibfried, B. E. King, and D. M. Meekhof. Experimental Issues in Coherent Quantum-State Manipulation of Trapped Atomic Ions. *Journal of Research of the National Institute of Standards and Technology*, 103(3):259–328, 1998.
- [13] John Preskill. Quantum computing in the nisq era and beyond. *Quantum*, 2:79, Aug 2018.
- [14] Christopher J. Foot. *Atomic Physics*. Oxford University Press, 2005.
- [15] Rainer Blatt, H Häffner, CF Roos, C Becher, and F Schmidt-Kaler. Ion trap quantum computing with Ca⁺ ions. *Quantum Information Processing*, 3(1-5):61–73, 2004.
- [16] B. K. Sahoo, Md. R. Islam, B. P. Das, R. K. Chaudhuri, and D. Mukherjee. Lifetimes of the metastable ${}^2D_{\frac{3}{2}, \frac{5}{2}}$ states in Ca⁺, Sr⁺, and Ba⁺. *Phys. Rev. A*, 74:062504, Dec 2006.
- [17] Winthrop W. Smith and Alan Gallagher. Radiative lifetime of the first ${}^2P_{\frac{3}{2}}$ state of ionized calcium and magnesium by the hanle effect. *Phys. Rev.*, 145:26–35, May 1966.
- [18] Wolfgang Paul and Helmut Steinwedel. Ein Neues Massenspektrometer Ohne Magnetfeld. *Zeitschrift Naturforschung Teil A*, 8:448, 07 1953.
- [19] F. Schmidt-Kaler, H. Häffner, S. Gulde, M. Riebe, G. P. T. Lancaster, T. Deuschle, C. Becher, W. Hänsel, J. Eschner, C. F. Roos, and R. Blatt. How to realize a universal quantum gate with trapped ions. *Applied Physics B: Lasers and Optics*, 77:789–796, 2003.
- [20] Daniel Rotter. Photoionisation von Kalzium. Master’s thesis, Universität Innsbruck, January 2003.
- [21] D. J. Wineland, R. E. Drullinger, and F. L. Walls. Radiation-pressure cooling of bound resonant absorbers. *Phys. Rev. Lett.*, 40:1639–1642, Jun 1978.
- [22] R. N. Gosselin, E. H. Pinnington, and W. Ansbacher. Measurement of the lifetimes of the 4P levels in Ca II using laser excitation of a fast beam. *Phys. Rev. A*, 38:4887–4890, Nov 1988.
- [23] Peter W. Shor. Polynomial-time algorithms for prime factorization and discrete logarithms on a quantum computer. *SIAM J. Comput.*, 26(5):1484–1509, October 1997.
- [24] P. Zeeman. *Over doubletten en tripletten in het spectrum teweeggebracht door uitwendige magnetische krachten*. Number Bd. 1 in *Over doubletten en tripletten in het spectrum teweeggebracht door uitwendige magnetische krachten*. Koninklijke Akademie van Wetenschappen, 1897.

- [25] P. Zeeman, Harvey B. Plotnick Collection of the History of Quantum Mechanics, and the Theory of Relativity. *Over den invloed eener magnetisatie op den aard van het door een stof uitgezonden licht*. Koninklijke Akademie van Wetenschappen te Amsterdam, 1896.
- [26] Michael Chwalla. *Precision spectroscopy with $^{40}\text{Ca}^+$ ions in a Paul trap*. PhD thesis, Universität Innsbruck, April 2009.
- [27] G. Tommaseo, T. Pfeil, Gita Revalde, G. Werth, Paul Indelicato, and J. Desclaux. The g_J -factor in the ground state of Ca^+ . *The European Physical Journal D - Atomic, Molecular, Optical and Plasma Physics*, 25, 08 2003.
- [28] Wolfgang Demtröder. *Experimentalphysik 3*, volume 4. Springer Berlin Heidelberg, 2010.
- [29] D. Leibfried, R. Blatt, C. Monroe, and D. Wineland. Quantum dynamics of single trapped ions. *Rev. Mod. Phys.*, 75:281–324, Mar 2003.
- [30] Christian Felix Roos. *Controlling the quantum state of trapped ions*. PhD thesis, Universität Innsbruck, 2000.
- [31] Paul Adrien Maurice Dirac and Ralph Howard Fowler. On the theory of quantum mechanics. *Proceedings of the Royal Society of London. Series A, Containing Papers of a Mathematical and Physical Character*, 112(762):661–677, 1926.
- [32] E. T. Jaynes and F. W. Cummings. Comparison of quantum and semiclassical radiation theories with application to the beam maser. *Proceedings of the IEEE*, 51(1):89–109, Jan 1963.
- [33] Thomas Monz. *Quantum information processing beyond ten ion-qubits*. PhD thesis, Universität Innsbruck, 2011.
- [34] Julian Rickert. Simultaneous and individual ion addressing for quantum information processing. Master’s thesis, Universität Innsbruck, 2018.
- [35] Philipp Schindler. Frequency synthesis and pulse shaping for quantum information processing with trapped ions. Master’s thesis, Universität Innsbruck, 2008.
- [36] I. I. Rabi. Space quantization in a gyrating magnetic field. *Phys. Rev.*, 51:652–654, Apr 1937.
- [37] Norman F. Ramsey. A molecular beam resonance method with separated oscillating fields. *Phys. Rev.*, 78:695–699, Jun 1950.
- [38] Romeo Alessandro Bianchetti. *Control and readout of a superconducting artificial atom*. PhD thesis, ETH Zürich, 2010.
- [39] David W. Allan, editor. *Statistics of Atomic Frequency Standards*, volume 54 of *Proceedings of the IEEE*, February 1966.
- [40] Roman Stricker. Gatteroperationen hoher Güte in einem optischen Quantenbit. Master’s thesis, Universität Innsbruck, 2017.

- [41] R. W. P. Drever, J. L. Hall, F. V. Kowalski, J. Hough, G. M. Ford, A. J. Munley, and H. Ward. Laser phase and frequency stabilization using an optical resonator. *Applied Physics B*, 31(2):97–105, Jun 1983.
- [42] Gerhard Kirchmair. Frequency stabilization of a Titanium-Sapphire laser for precision spectroscopy on Calcium ions. Master’s thesis, Universität Innsbruck, November 2006.
- [43] Judah Levine. *Measuring Time and Comparing Clocks*. NIST and the University of Colorado, April 2016.
- [44] N. Huntemann, C. Sanner, B. Lipphardt, Chr. Tamm, and E. Peik. Single-ion atomic clock with 3×10^{-18} systematic uncertainty. *Phys. Rev. Lett.*, 116:063001, Feb 2016.
- [45] S. M. Brewer, J.-S. Chen, A. M. Hankin, E. R. Clements, C. W. Chou, D. J. Wineland, D. B. Hume, and D. R. Leibbrandt. $^{27}\text{Al}^+$ quantum-logic clock with a systematic uncertainty below 10^{-18} . *Phys. Rev. Lett.*, 123:033201, Jul 2019.
- [46] I. I. Rabi, J. R. Zacharias, S. Millman, and P. Kusch. A new method of measuring nuclear magnetic moment. *Phys. Rev.*, 53:318–318, Feb 1938.
- [47] Jake VanderPlas. Frequentism and Bayesianism: A Python-driven Primer. *arXiv*, *arXiv:1411.5018[astro-ph.IM]*, 2014.
- [48] Adriene Marie Legendre. Nouvelles méthodes pour la détermination des orbites des comètes. Paris, 1805. cited in Manseld Merriman, *On the history of the method of least squares*. *The Analyst*, 4(2):3336, 1877.
- [49] Robert Adrain. Research concerning the probabilities of the errors which happen in making observation. In *The Analyst*, 1808. cited in Manseld Merriman, *On the history of the method of least squares*. *The Analyst*, 4(2):3336, 1877.
- [50] Carl Friedrich Gauss. *Theoria motus corporum coelestium in sectionibus conicis solem ambientium*. Perthes et Besser, Hamburg, 1809. Translated into German by C. Haase as *Theorie der Bewegung der Himmelskörper welche in Kegelschnitten die Sonne umlaufen*, Hannover, 1865.
- [51] Pierre-Simon Laplace. Mémoire sur les intégrales définies, et leur application aux probabilités, et spécialement à la recherche du milieu qu’il faut choisir entre les résultats des observations. In *Mémoires de l’Institut National des Sciences et Arts*, 1810. cited in Manseld Merriman, *On the history of the method of least squares*. *The Analyst*, 4(2):3336, 1877.
- [52] Thomas Bayes and Richard Price. An Essay towards solving a Problem in the Doctrine of Chances. By the late Rev. Mr. Bayes, F. R. S. communicated by Mr. Price, in a Letter to John Canton, A. M. F. R. S. *Philosophical Transactions of the Royal Society of London*, 1763.

- [53] Pierre-Simon Laplace. Mémoires sur les suites récurro-récurrentes et sur leurs usages dans la théorie des hasards. In *Mémoires de mathématique et de physique présentés à l'Académie royale des sciences, par divers savans, & lûs dans ses assemblées*, 1774. cited in Stephen M. Stigler, *Laplace's 1774 Memoir on Inverse Probability*. *Statistical Science*, 1(3):359–363, 1986.
- [54] James Joyce. Bayes' Theorem. In Edward N. Zalta, editor, *The Stanford Encyclopedia of Philosophy*. Metaphysics Research Lab, Stanford University, spring 2019 edition, 2019.
- [55] Daniel Zwillinger and Stephen Kokoska. *CRC standard probability and Statistics tables and formulae*. Chapman and Hall/CRC, 2000.
- [56] Subhash Bagui and K. L. Mehra. Convergence of Binomial to Normal: Multiple Proofs. *International Mathematical Forum*, 12(9):399–411, 2017.
- [57] Kenneth Levenberg. A Method for the Solution of Certain Non-Linear Problems in Least Squares, 1944.
- [58] Donald W. Marquardt. An Algorithm for Least-Squares Estimation of Nonlinear Parameters. *Journal of the Society for Industrial and Applied Mathematics*, 11(2):431–441, 1963.
- [59] Y. Huang, H. Guan, P. Liu, W. Bian, L. Ma, K. Liang, T. Li, and K. Gao. Frequency Comparison of Two $^{40}\text{Ca}^+$ Optical Clocks with an Uncertainty at the 10^{-17} Level. *Phys. Rev. Lett.*, 116:013001, Jan 2016.
- [60] Ethan. Bernstein and Umesh. Vazirani. Quantum complexity theory. *SIAM Journal on Computing*, 26(5):1411–1473, 1997.
- [61] Quantencomputer in der Cloud, September 2019. <https://www.uibk.ac.at/newsroom/quantencomputer-in-der-cloud.html.de>, accessed on 18.10.2019.
- [62] Vlad Negnevitsky. *Feedback-stabilised quantum states in a mixed-species ion system*. PhD thesis, ETH Zürich, 2018.
- [63] X. Fu, L. Riesebos, L. Lao, C. G. Almudever, F. Sebastiano, R. Versluis, E. Charbon, and K. Bertels. A heterogeneous quantum computer architecture. In *Proceedings of the ACM International Conference on Computing Frontiers*, CF '16, pages 323–330, New York, NY, USA, 2016. ACM.
- [64] David C. McKay, Thomas Alexander, Luciano Bello, Michael J. Biercuk, Lev Bishop, Jiayin Chen, Jerry M. Chow, Antonio D. Córcoles, Daniel Egger, Stefan Filipp, Juan Gomez, Michael Hush, Ali Javadi-Abhari, Diego Moreda, Paul Nation, Brent Paulovicks, Erick Winston, Christopher J. Wood, James Wootton, and Jay M. Gambetta. Qiskit Backend Specifications for OpenQASM and OpenPulse Experiments, 2018.
- [65] Gidney Craig, Bacon Dave, and contributors. Cirq. <https://github.com/quantumlib/Cirq>, January 2018.

- [66] ECMA International. Ecma-404: The json data interchange syntax, December 2017.
- [67] Dick Hardt. RFC 6749. - The OAuth 2.0 Authorization Framework. Errata: RFC 6749, October 2012.
- [68] Dick Hardt and Michael Jones. RFC 6750. - The OAuth 2.0 Authorization Framework: Bearer Token Usage. Errata: RFC 6750, October 2012.
- [69] Craig Gidney, Wojciech Mruczkiewicz, Dave Bacon, and Andreas Bengtsson. Implementation of the Bernstein-Vazirani algorithm in Cirq, February 2019. https://github.com/quantumlib/Cirq/blob/master/examples/bernstein_vazirani.py, accessed on 18.10.2019.
- [70] Atos Quantum Learning Machine Brochure, July 2018. <https://atos.net/wp-content/uploads/2018/07/Atos-Quantum-Learning-Machine-Brochure.pdf>, accessed on 18.10.2019.
- [71] Mølmer, Klaus and Sørensen, Anders. Multiparticle Entanglement of Hot Trapped Ions. *Physical Review Letters*, 82(9):1835–1838, Mar 1999.